CHARACTERISATION OF SOFT MAGNETIC COMPOSITES

RajeshKrishnan Neethirajan

LUTMDN/(TMMV-5378)/1-46/2025

May 2025

Division of Production and Materials Engineering

Department of Industrial and Mechanical Sciences, LTH, Faculty of Engineering

Lund University

Supervisor: Prof. Dmytro Orlov, Lund University

Co-Supervisor: Pontus Fyhr , Alvier Mechatronics

Examiner: A/Prof. Filip Lenrick, Lund University

Abstract

Soft Magnetic Composites (SMCs) represent a new generation of materials gaining attention for their effective use in electric motors and transformers. The strong magnetic properties, reduced eddy current losses, and flexibility in forming complex 3D shapes. They offer clear advantages over traditional laminated steels, especially in the designs where magnetic behavior is needed in all directions. SMCs are made from iron particles coated with an insulating layer, offer a unique combination of design flexibility and functional efficiency, making them well-suited for complex electromagnetic applications. This study focuses on exploring the microstructure and porosity of SMCs, aiming to better understand and improve their role in electromagnetic systems, particularly in motor component applications. The analysis of SMC materials fabricated through conventional die compaction methods, using high-purity iron powder coated with insulating layers. Samples were subjected to systematic surface preparation and examined using digital optical microscopy combined with image processing techniques in ImageJ. Quantitative parameters such as particle size, coating area, and pore equivalent diameter were extracted from nine distinct regions across the samples. The results reveal significant Variation across regions. This non-uniformity affects the electromagnetic properties of SMCs, but also suggests unequal pressure distribution during compaction. These findings provide valuable insight into optimizing compaction parameters and improving the homogeneity and functional performance of soft magnetic materials.

Acknowledgment

This thesis would not have been possible without the support and guidance of many individuals and institutions. First and foremost, I extend my heartfelt gratitude to Prof. Dmytro Orlov, my supervisor at Lund University, for his invaluable insights, constructive feedback, and consistent encouragement throughout this project. His expertise in materials engineering and support during the experimental stages were crucial for the successful completion of this work.

I would also like to thank my co-supervisors, Pontus Fyhr and Hans-Göran Künkel, both from Alvier Mechatronics, for their technical support, guidance, and valuable input throughout the research. Their combined industry knowledge and practical perspective were instrumental in shaping the direction of this work.

Special thanks go to Höganäs AB for generously providing the material samples used in this study.

I am deeply grateful to A/Prof. Filip Lenrick, the examiner for this thesis, for his review and feedback that helped elevate the quality of the work.

I wish to express appreciation to the Division of Production and Materials Engineering, LTH, Faculty of Engineering, Lund University, for offering access to laboratory facilities and analytical tools, particularly the Digital optical microscope and ImageJ software that were integral to this study.

Special thanks go to Johan Ranstad, whose guidance and professional support during the project were greatly appreciated.

Finally, I would like to thank my Family and Friends for their continuous encouragement, understanding, and support throughout this academic journey.

Author Declaration

The paraphrasing tool Quillbot was used in this report to enhance the language and improve the overall flow.

List of Figures

Contents

1. Introduction

As the global push toward electrification accelerates, the demand for high-efficiency electric motors has brought increased attention to the materials used in magnetic core components [1][2]. Among emerging alternatives to conventional laminated steels are Soft Magnetic Composites (SMC) materials made from ferromagnetic iron particles coated with electrically insulating layers [3]. These composites offer advantages, including three-dimensional isotropic magnetic properties, reduced eddy current losses, and the ability to form complex geometries, making them especially appealing for next-generation electrical machines [4].

Höganäs AB has developed advanced SMC materials such as SOMALOY 700 HR 5P [5]. These are designed to meet the performance demands of modern electrical systems [6]. However, achieving the desired performance depends heavily on precise processing and structural consistency [7]. A major challenge is controlling density and porosity variations that occur during powder compaction [8,9,10]. These variations can significantly influence the final properties of the material, particularly in terms of magnetic losses and mechanical strength [11,12,13,14].

The study focuses on the microstructural characterization of SMCs specifically looking at particle morphology, coating uniformity, and porosity distribution across different regions of compacted samples. By using digital optical microscopy combined with quantitative image analysis, we aim to assess how microstructural features vary locally and how these variations relate to compaction parameters and overall processing conditions.

Thus, the aims of this thesis are to:

1. Analyze the distribution and morphology of particles within each region to assess how packing behavior and deformation during pressing affect local structure.

2. Evaluate the uniformity of the insulating coating on individual particles, which is critical for minimizing eddy current losses in electromagnetic applications.

3. Investigate how porosity levels vary across different regions of the SMC samples with a focus on identifying any systematic gradients introduced during compaction.

4. Compare results across multiple samples to determine whether observed trends are consistent and repeatable, and what they reveal about overall process reliability and manufacturing uniformity.

2 Literature survey

2.1 Basic principles of electric motor design

An electric motor is used to convert electric energy from an Alternating current (AC) or Direct current (DC) to the mechanical energy at the rotating shaft. There are several types of electric motors such as induction motors, synchronous motors, and DC motors [15,16,17]. The automotive industry shifts toward electrification creates the demand for efficient compact and high-torque electric motors increasing rapidly [18,19]. In modern automobiles, electric vehicles (EVs) and hybrid electric vehicles (HEVs), electric motors are fundamental components that drive propulsion and auxiliary systems. Two main motors that are widely adopted in automotive applications are Radial Flux Motors (RFMs) and Axial Flux Motors (AFMs) (Figure 1). Each has specific advantages in terms of packaging, cooling, and performance [20,21]. The basic principle of an electric motor is that current-carrying windings generate motion, with the current being supplied either through direct conduction or induced by electromagnetic induction [22] All electric motors have basic features such as stationary member stator and rotating member rotor. The stator and rotor have laminated magnetic cores composed of copper or aluminum windings (Figure 1). The stator is the critical component of an electric motor, which generates the rotating magnetic field driving the motor [22,23,24].

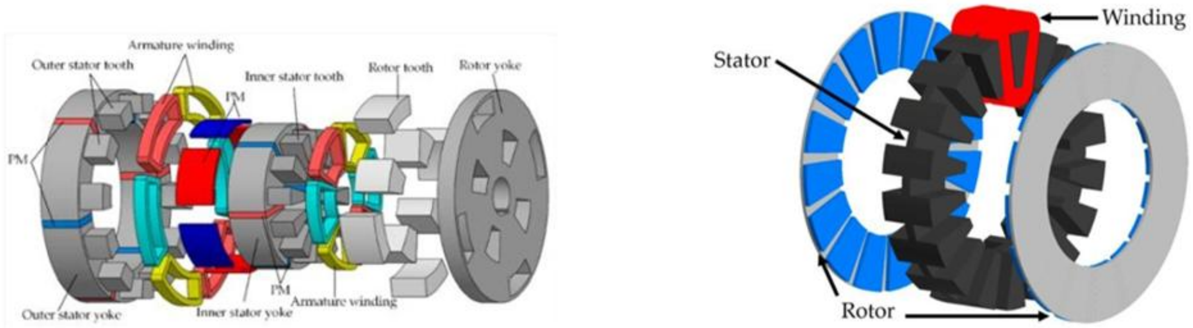

Figure 1.Exploded views of axial flux machine assemblies. (A) dual-rotor, with the key components including the rotor yoke, stator teeth, armature windings, permanent magnets (PM), and yoke structures (Zhang et al., 2022). Core components (B): stator, rotor, and winding arrangement (Credo et al., 2021).

In a stator, laminated electrical steel (LES) and SMCs are two key materials, each with distinct advantages. LES offers high magnetic saturation, better thermal conductivity, and is well-suited for 2D magnetic flux paths. By contrast, SMCs provide isotropic magnetic properties, very low eddy current losses, and enable complex 3D geometries [25,26,27]. SMC becomes advantageous due to their compactness, low loss at high frequencies, and flexible 3D shaping, which is a priority in modern EV stators where innovative designs are common [28,29].

Selecting appropriate materials is critical for ensuring optimal performance in magnetic applications, with distinct considerations necessary for AC and DC systems [30,31]. The magnetic behavior of powders is influenced by multiple factors, including their chemical composition, melting and hardening practices, and post-processing heat treatments. Magnetically soft alloys used in such applications are expected to exhibit several key properties [30,32,33], such as:

1. Low hysteresis losses
2. Low eddy current losses
3. High permeability at low field strengths
4. High saturation magnetization
5. Consistency in magnetic characteristics across samples

2.2 Introduction of soft magnetic composites

Soft Magnetic Composites consist of ferromagnetic powder particles individually coated with electrically insulating layer (Figure 2). This unique structure allows for improved magnetic performance, particularly in applications involving complex magnetic flux paths [30]. SMCs are broadly used in both DC and AC applications [30,34]. In the context of electrical machines, SMCs are especially suitable for radial and axial flux topologies due to their ability to provide three-dimensional isotropic magnetic behavior [30,35]. Unlike laminated steels, which restrict magnetic flux paths to planar directions, SMCs provide enhanced magnetic circuit flexibility, making them particularly suitable for manufacturing complex stator ring geometries in axial and radial flux machines. These composites are used in core designs for brushless DC motors, switched reluctance motors, and high-efficiency radial or axial flux machines [30,35,36].

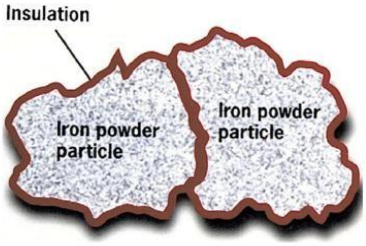

Figure 2.: Iron particle with insulating coating Adapted from [6].

2.2.1 Common materials for SMC

Pure iron is the most commonly used material for (SMCs) Common alloying elements include Aluminium (Al), Silicon (Si), Chromium (Cr), Niobium (Nb), Molybdenum (Mo), Nickel (Ni), and Cobalt (Co) added in concentrations up to approximately 20 wt%. These elements help improve magnetic permeability and lower core losses, which increase the overall efficiency of the material. However, even though alloying improves resistivity, eddy current losses can still be an issue especially at standard industrial frequencies like 50 Hz.[30].

2.2.2 Pure iron

Pure iron is also known as electrical iron, which is a low-carbon material with very good soft magnetic properties [30]. It has slightly higher magnetic permeability than iron cobalt alloys. It is often used in relays, solenoids, and magnetic parts in vacuum equipment, especially for DC use. For critical applications, powder metallurgy is used to produce high-purity iron powders with minimal amounts of carbon, sulfur, oxygen, and hydrogen [30,31].

2.2.3 Fe–Ni alloys

Iron–nickel (Fe–Ni) alloys have the highest magnetic permeability of all soft magnetic materials, though their saturation flux density is usually lower than that of other alloys. They are ideal for applications that need very high permeability and can manage with lower magnetic induction. The magnetic properties of these alloys vary with their composition, so the nickel content needs to be chosen carefully [30,32].

2.2.4 Fe–Si alloys

Fe–Si alloys are commonly used in applications with alternating magnetic fields because they offer better electrical resistivity and magnetic performance than pure iron. These are mainly used in devices like relays, transformers, and solenoids, with low hysteresis loss, high permeability, and good electrical resistance [30,33].

2.3.5 Fe–Co alloys

Among all the soft magnetic materials, Iron–cobalt (Fe–Co) alloys have the highest magnetic saturation, which makes it suitable for use in places where maximum magnetic flux is required. These are also used for the creation of compact, high-efficiency magnetic circuits. Further, these alloys can be found in aerospace components, motors, generators, magnetic bearings, and advanced transformers. Thus, their ability to handle high magnetic flux is essential for energy transfer [30,34].

2.3 Fabrication Techniques for soft magnetic composites

2.3.1 Powder preparation

Powder preparation is the main step in powder metallurgy. This involves the production of metal powders for subsequent processing. The methods used for powder production are classified into chemical, physical, and mechanical techniques. Chemical methods include chemical reduction of metal oxides and decomposition of compounds like metal hydrides and carbonyls. Physical methods involve processes like electrolytic deposition, which gives high purity powders and atomization with gas, water, centrifugal, cryogenic, or vacuum that breaks molten metal into fine particles. Mechanical methods, such as ball milling, are mainly used for brittle or reactive materials, producing powders by grinding or crushing [8,35].

2.3.2 Insulating Coatings

Coated iron-based powders consist of essentially pure iron particles encapsulated by a thin, electrically insulating layer [8][30][36]. The primary objective of the coating is to suppress eddy current losses, especially in high-frequency applications. At lower frequencies, while insulation is somewhat less critical, it still plays a key role in minimizing eddy current effects that degrade the magnetic performance [37]. There are two principal coating technologies used in the industry: Liquid Coating Technology and Powder Coating Technology. Insulating coatings can be divided into organic and inorganic coatings. Organic coatings include thermoplastics and thermosetting polymers, which serve as binders and insulators. The volume of non-magnetic polymer should be reduced in order to maintain high magnetic permeability, which maximizes the iron content [38].

Inorganic coatings commonly include metallic oxides, phosphates, and sulfates. These coatings provide high thermal stability and are particularly suited for high-temperature sintering processes [39]. Inorganic coatings are applied using two general methods. Wet Chemical Method (WCM) involves immersing particles in a chemical bath where an inorganic layer precipitates on the surface. This method requires strict control of bath composition, temperature, and treatment time, as powder particles are more reactive and harder to coat uniformly than bulk materials. Dry Chemical Method (DCM) is conducted in a controlled furnace environment where powders are oxidized at elevated temperatures, forming a thin oxide or phosphate layer. Phosphate coatings are the most widely used inorganic coatings in soft magnetic composites and can be applied via immersion, spraying, or mechanical alloying. The choice between zinc, iron, or manganese phosphate depends on the desired magnetic and mechanical performance [40].

2.3.3 Powder Compaction Techniques

The compaction of metal powders plays a crucial role in powder metallurgy which serves to consolidate the powder into the desired shape to achieve near-final dimensions with consideration for changes during sintering, control the level and type of porosity, and impart sufficient strength for handling in subsequent processing steps[41,42,43,44]. The metal powder compaction is broadly classified based on process continuity, magnitude of applied pressure, compaction velocity, processing temperature and the method of pressure application [45,46] .The pressing operations can be sequenced as Filling of the die cavities with the required quantity of powder followed by Pressing operation in order to achieve required green density and part thickness and withdrawal of the upper punch from the compact (Figure 3). P/M parts usually are classified by evaluating the complexity of part design on a range which are Single level components with the compacting force applied from one direction only. In this case the part thickness is generally limited to a maximum of 6–7 mm. Single level components with the force applied from two directions. Two level components pressed with forces from two directions. Multilevel parts pressed with forces from two directions [4,30, 45].

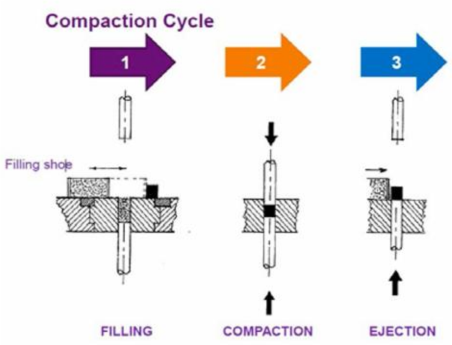

Figure 3.Schematic representation of the compaction cycle in powder metallurgy. Adapted from [6]

2.3.4 Die Compaction

This involves rigid dies and mechanical or hydraulic presses. Densities up to 90 % of full density can be achieved following the compaction cycle [4,46]. The friction between the powder and die wall and between individual powder particles hinders pressure transmission [4,47,48,49,50,51]. A high uniformity in green parts can be achieved depending on the kind of compacting technique which is type of tools and the materials to be pressed with the lubricant [4,52,53]. The compacting techniques would be characterized by references to the movement of the individual tool elements which is upper punch, lower punch and die relative to one another. The Pressing within fixed dies can be divided into Single action pressing and Double action pressing. The pressing operation is carried out by the upper punch as it moves into the fixed die. The die wall friction prevents uniform pressure distribution. The compact has a higher density on top than on the bottom. The another type of pressing only the die is stationary in the press. Upper and lower punches advance simultaneously from above and below into the die. The consequence is high density at the top and undersides of the compact. In the center there remains a neutral zone which is relatively weak [4,48,50,54,55].

2.3.5 Factors Affecting the Compaction Process

The compaction process in powder metallurgy is influenced by factors that determine the density, strength, and integrity of the green compact [56,57,58]. Powder characteristics like particle size, shape, distribution, and surface roughness affect packing behavior and followability. The finer particles may improve green density and interlocking but can also increase friction and tool wear[59,60]. Lubricants are essential for reducing die wall friction, ensuring smooth ejection, minimizing tool wear, and promoting uniform density, though improper application can lead to defects like cracking. Additionally, compaction pressure and speed must be carefully controlled[61,62]. The higher pressures improve densification but may cause structural defects if over-applied, while compaction speed affects particle rearrangement and uniformity, with high-speed pressing favoring productivity and slower speeds enhancing consistency. Balancing all these factors is essential to optimize compaction performance [63,64].

2.4 Magnetic property characterization

SMCs possess a unique combination of magnetic and thermal isotropy, making them highly suitable for modern electromagnetic applications [65,66]. Their advantages include extremely low eddy current losses, low total core losses over a broad frequency range, high magnetic permeability, and elevated magnetization. These materials also offer high electrical resistivity, reduced weight and volume, low coercivity, a large anisotropy constant, and high Curie temperatures. Despite their advantages, SMCs have limitations. Although they can achieve high permeability and induction, these properties may still fall short when compared to laminated steel cores [67,68]. Furthermore, the powder metallurgy process used to produce soft magnetic powder cores is not always suitable for all component shapes and sizes [69,70]. Different magnetic materials are used across frequency ranges depending on their characteristics. The soft ferrites perform well in high-frequency applications due to low core losses but suffer from low magnetic flux density, requiring larger cores. Electrical steel sheets offer higher flux density but become inefficient at high frequencies due to significant core losses [71,72,73]. Powder cores, such as SMCs, bridge the performance gap between ferrites and electrical steels, performing effectively where neither of the other two materials.

2.4.1 Core loss

Core losses, also known as iron losses, are energy losses that occur within the magnetic core of the electric motor. It typically occurs because of hysteresis and eddy currents in the iron core (Figure4). Core losses are essential to address because they directly impact a motor's efficiency [74,75,76]. SMCs offer low core losses at high frequencies, making them ideal for high-speed electronic components [77]. The total core loss P_t magnetic device is the sum of the eddy current losses P_e and hysteresis losses P_h

$$P_t = P_e + P_h$$

2.4.2 Hysteresis loss

Hysteresis loss is the main core loss at low frequency. It can be reduced by larger particle size and higher purity of the iron in the particles and stress relieving heat treatment [78].

$$P_h = f \oint HdB$$

Where Ph is the hysteresis loss, f is the frequency, H is the magnetic field strength, and B is the magnetic induction. In an iron powder material, impurities in the iron particles and stressed regions give rise to pinning sites that hinder domain wall motion. The coercive force raised by these causes can be reduced by using a high purity iron for the particles and providing a heat treatment procedure following compaction to improve the stressed regions. Another source of hindering the domain wall motion is possible grain boundaries inside the particles. The heat treatment procedure following the compaction is the main step to be taken to reduce hysteresis loss [79,80].

2.4.3 Eddy current loss

Eddy current loss is due to electrical resistance losses within the core caused by the alternating electric field. When eddy currents are induced in materials, two main effects are observed incomplete magnetization of the material and increase in core losses [81]. Eddy current loss can be expressed as

$$P_e = \frac{CB^2 f^2 d^2}{\rho}$$

B the flux density, f is the frequency, ρ the resistivity, and d is the thickness of the material. The latest technique is insulated iron powder with the smallest eddy current loss. The insulating coating of every particle gives very small eddy current paths inside a particle and a relatively high resistivity of the bulk material [82]. The small non-magnetic distances between every particle act as air gaps and decrease the permeability of the bulk material [83].

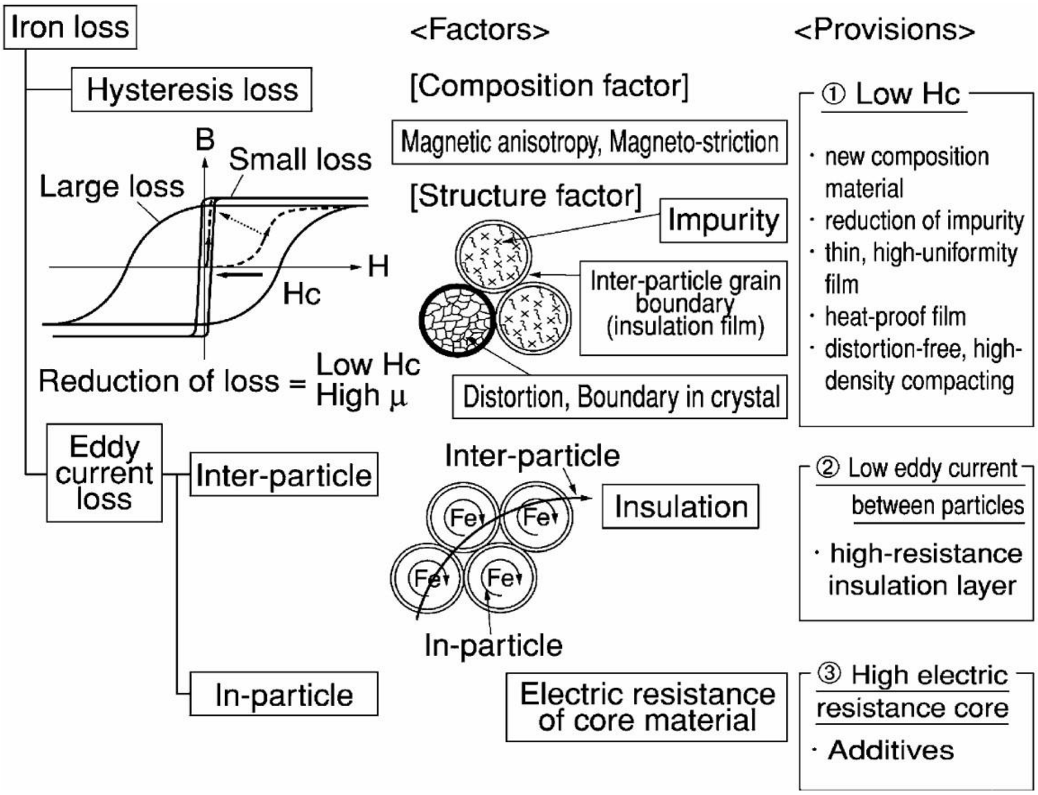

Figure 4. Schematic illustration of iron loss mechanisms in soft magnetic composites and the corresponding factors and provisions for loss reduction. Adapted from [6]

2.4.4 Magnetic Permeability

The essential performance indicators for iron core components are magnetic permeability. These magnetic, electrical, and mechanical properties are significantly influenced by the processing methods and preparation techniques used during component fabrication. Additionally, the purity of the raw materials, along with the shape and size of the particles, plays a critical role in determining the final magnetic response of the material [84].SMCs can be effectively described by its permeability because it directly links two main magnetic quantities the magnetic field strength H and flux density B

$$B=\mu H$$

There are different ways to understand magnetic permeability. One way is by looking at DC permeability, which describes how much magnetic field (B) is created in a material when it's exposed to a constant, unchanging magnetic force (H). Such effect is related to the movement of magnetic domain walls and is a function of the material's features as well as external factors. The concept of permeability is also useful to deal with SMCs exposed to AC conditions [85].

2.5Microstructural Analyses

2.5.1Optical Microscopy

Optical Microscopy (OM) is often employed as a primary technique for the analysis of sample surface features. The principal feature of OM lies in the ability to capture the images formed by the passage of light beams through the sequence of optical elements used in the pixel matrix Figure (5)[86,87]. This method provides visually examining microstructural details, such as Iron Particle shape and size, insulating coating and surface defects. Additionally, multiple images can be stitched to create a comprehensive view of a larger area.

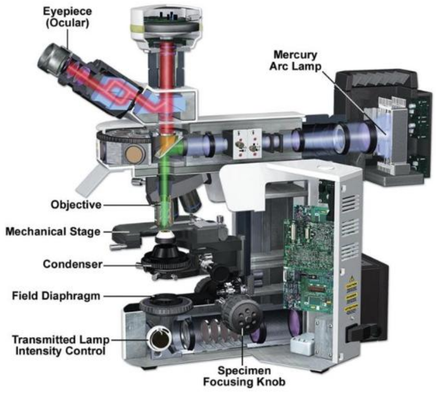

Figure 5.Schematic diagram of a modern optical microscope system, illustrating the light path and key components including the light source, condenser, objective lens, and digital camera. Adapted from [86].

2.5.2 Image analysis:

The micrographs captured through optical microscopy were processed using digital image analysis to extract meaningful structural information [88,89]. Brightness adjustment and contrast were adjusted, along with smoothing or sharpening filters, which helped prepare the images for segmentation. Thresholding was used, which allowed clear separation of features such as particles, pores, and coatings from the background. The analysis was carried out using ImageJ, a widely used open-source software, which enables accurate measurement of microstructural properties. The software was used to evaluate particle size, shape, and orientation, as well as pore size, shape, orientation, and distribution. It also allowed for quantifying the coating area fraction and its distribution across the sample. These measurements, obtained through segmentation and particle analysis tools, provided valuable insights into the material’s internal structure and gave a better understanding of how these microstructural features influence its overall behavior [90].

Although SMCs have been widely investigated for their unique combination of magnetic and mechanical properties, most existing studies emphasize bulk magnetic behavior. There is limited research that systematically examines how regional inconsistencies such as particle distribution, porosity gradients, and coating uniformity affect the internal quality of geometrically complex components like stator teeth. Further, the influence of die geometry and compaction technique on regional microstructural features has been explored only in recent times, especially for stator-ring and cube-shaped samples. This gap highlights the need for detailed location specific microstructural analysis to have a better understanding and optimization of the fabrication process for SMC components.

3. MATERIALS AND METHODS:

Samples in the form of stator tooth and cubes were manufactured in the fixed dies with single action pressing and double action pressing at Höganäs. The analysis of their microstructure was performed at Lund University.

3.1 Specimen preparation

In this study, the material selected for experimentation is SOMALOY 700 HR 5P. This alloy is composed of high-purity iron powder with particle sizes ranging from 50 to 150 µm. Each particle is coated with a phosphate-based insulating layer with additives 0.3% 5p lube, as indicated in (Table 1)

samples	Type	Dimension (mm)
1	Stator	24x20x6
2	Stator	24x20x6
3	Cube	22x22x10

Table 1. Sample specifications and physical dimensions used for microstructural analysis.

The compaction was carried out under a uniaxial pressure of 800 MPa with the die maintained at a temperature of 100 °C. This was followed by a heat treatment conducted in a nitrogen atmosphere at 650 °C. The preparation of samples started with the computer Aided Design (CAD) and the parameters are shown in the (Table 2) below along with coordination system schematic, as shown in (Figure 6).

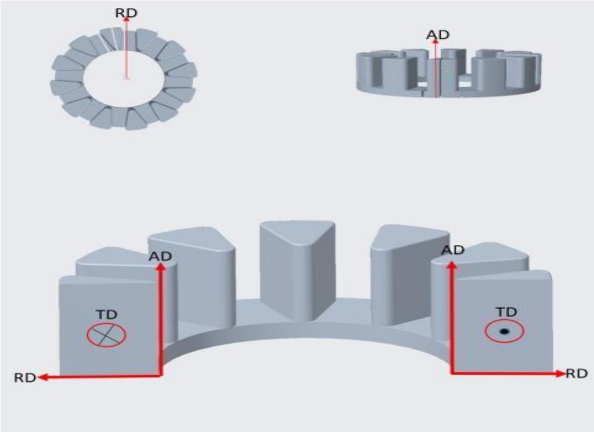

Figure 6. CAD model of the stator ring illustrating geometric directions such as axial direction (AD) Radial direction (RD) and Tangential direction (TD)

Parameter	Value	unit
Tooth number	12	
Outer Diameter	109.7	mm
Inner Diameter	60	mm
Axial length	24	mm
Radial Height	20	mm
Core back depth	5	mm

Table 2.CAD based dimensional parameters for stator geometry design used in sample preparation

The preparation of the stator and cube specimens involved a multi-stage cutting and finishing process to ensure high-quality surface for microstructural analysis (Figure 7). Initial sectioning of the stator rings was performed using a diamond wire saw with a wire speed of 2.0 m/s, a feed force of 150 g, wire tension of 1500 g, and a wire diameter of 0.22 mm. Water was used as a coolant to minimize thermal effects and assist in debris removal. Following this, stator rings were mounted on a precision abrasive cut-off machine to bisect individual teeth with a dimensional tolerance of ±1 mm, while cube specimens were directly sectioned using the same machine. The cutting process employed an aluminum oxide grinding wheel (50A15) with dimensions of 15 mm × 0.5 mm × 12.7 mm, operating at 3000 rpm with a feed rate of 0.01 mm/s, and water as a coolant to prevent thermal damage and enhance surface quality. Subsequent surface grinding was carried out using silicon carbide (SiC) abrasive papers in sequential grit sizes of P800, P1200, P2000, and P4000. After each grinding step, specimens were rinsed thoroughly with water to eliminate residual abrasive particles and prevent contamination between stages. Final polishing was completed using diamond suspension sprays of 3 µm (M3), 1 µm (M1), and 0.25 µm (P1/4) applied to a cloth-covered polishing wheel, achieving a mirror-like finish while minimizing deformation caused during grinding.

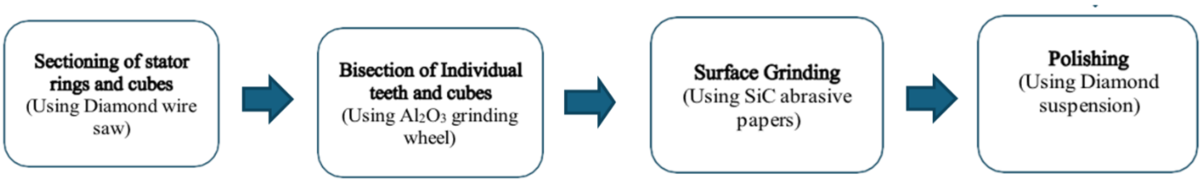

Figure 7. Flow chart illustrating the multi-stage preparation process for stator and cube specimens

3.2 Digital Optical Microscopy

The OM, was used for digital image acquisition and processing to extract quantitative information from microstructural images. As light passes through or reflects off from the sample surface, intensity variations caused by surface features such as particles, pores, and coatings are collected by the objective lens and directed through semi-reflecting mirrors toward the photographic sensor (Figure 8). These variations are recorded as pixel intensity differences in the resulting digital image, enabling quantitative analysis of microstructural characteristics such as particle size, pore distribution, and coating coverage.

To investigate the microstructural characteristics of the samples, digital optical microscopy was performed using a Keyence VHX-6000 system. Images were acquired from selected Nine locations across each sample. Specifically, micrographs were captured from top, middle, and bottom, each further divided into left, center, and right were selected for imaging. This approach was chosen due to density variations during the manufacturing or processing gradients.

A fixed magnification and scale bar were applied to all images to maintain consistency. For the sample overview image magnification of 200x and scale bar of 1000 micrometer and location specific image was taken with the magnification of 300x and scale bar of 100 micrometer for the stator samples and magnification 500x and scale bar of 100 micrometer The scale was chosen to ensure that a sufficient number of microstructural features such as particles, pores, and coating interfaces were visible within each field of view. This allowed for statistical significance in the subsequent image analysis, with each frame containing multiple repeatable features for accurate quantitative evaluation.

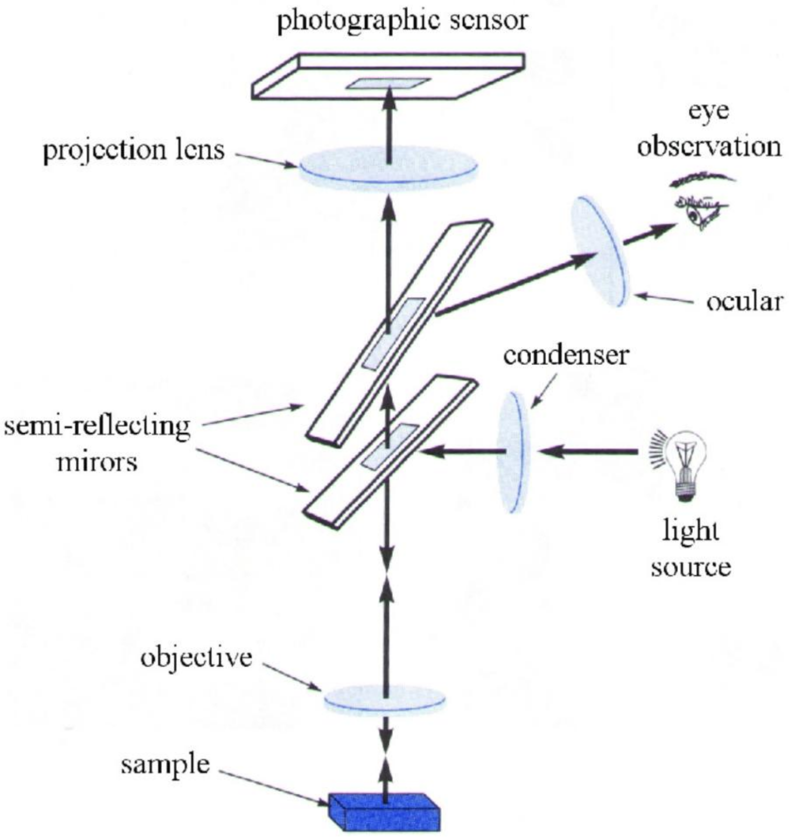

Figure 8. Schematic diagram illustrating the basic working principle of an optical microscope used in digital image acquisition. Adapted from [87]

3.3 Digital image processing

The image taken from the microscopy was qualitatively analyzed through the digital image processing technique (Figure 9). The optical image was calibrated in a line drawn over the scale bar present in the micrograph which allows the software to accurately convert pixel measurements into micrometers. Images were converted to a 8-bit grayscale format using the ImageJ software, to standardize the intensity values across all samples and facilitate uniform processing.

Subsequently, image segmentation was performed using Thresholding techniques to convert the grayscale images into binary form. Through this approach, grayscale images were converted into binary images, enabling clear differentiation between features of interest and background. This process involves distinguishing and isolating features such as particles, binders, and pores from the background matrix. Thresholding was applied using both manual adjustment and automated algorithms, with the Otsu method frequently employed due to clear separation between phases. To minimize high-frequency noise while preserving edge information between adjacent features such as grains or pores, a Gaussian filter with a sigma value of 2 was applied. The selection of the filter size was made carefully, considering the trade-off between effective noise reduction and the potential distortion of fine features.

Following Thresholding, the binary images were refined using a median filter to further suppress noise and improve the clarity of feature boundaries. Once the phase separation was complete, each particle or pore was represented as a distinct connected group of pixels. Quantitative analysis was then performed to extract features such as Area fraction, equivalent diameter. A size filter was also applied to eliminate noise and irrelevant small features by setting a minimum area threshold, ensuring only statistically significant elements were included in the analysis.

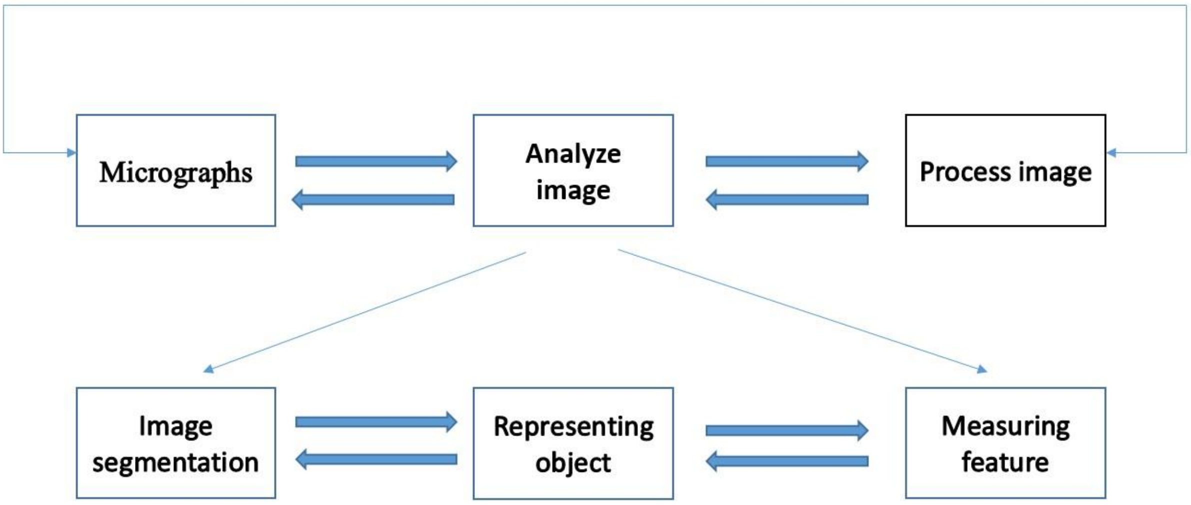

Figure 9.Flowchart illustrating the image processing workflow used for microstructural analysis of soft magnetic composites

4. Results and Analysis

4.1 Sample overview

The SMC samples are analyzed for the distribution of pores, particle morphology, and coating layers (Figure 10). To ensure a comprehensive analysis. Nine distinct locations across the surface of the sample- top, middle, and bottom, each further divided into left, center, and right are selected for imaging and evaluation using optical microscopy (Figure 11). These locations are strategically chosen to cover different regions of the sample, minimizing location bias and for the assessment of local variations in compaction density, pore size, particle distribution, and coating uniformity [91]. Quantitative analysis is performed using ImageJ software to extract data on particle area, pore area, and coating characteristics.

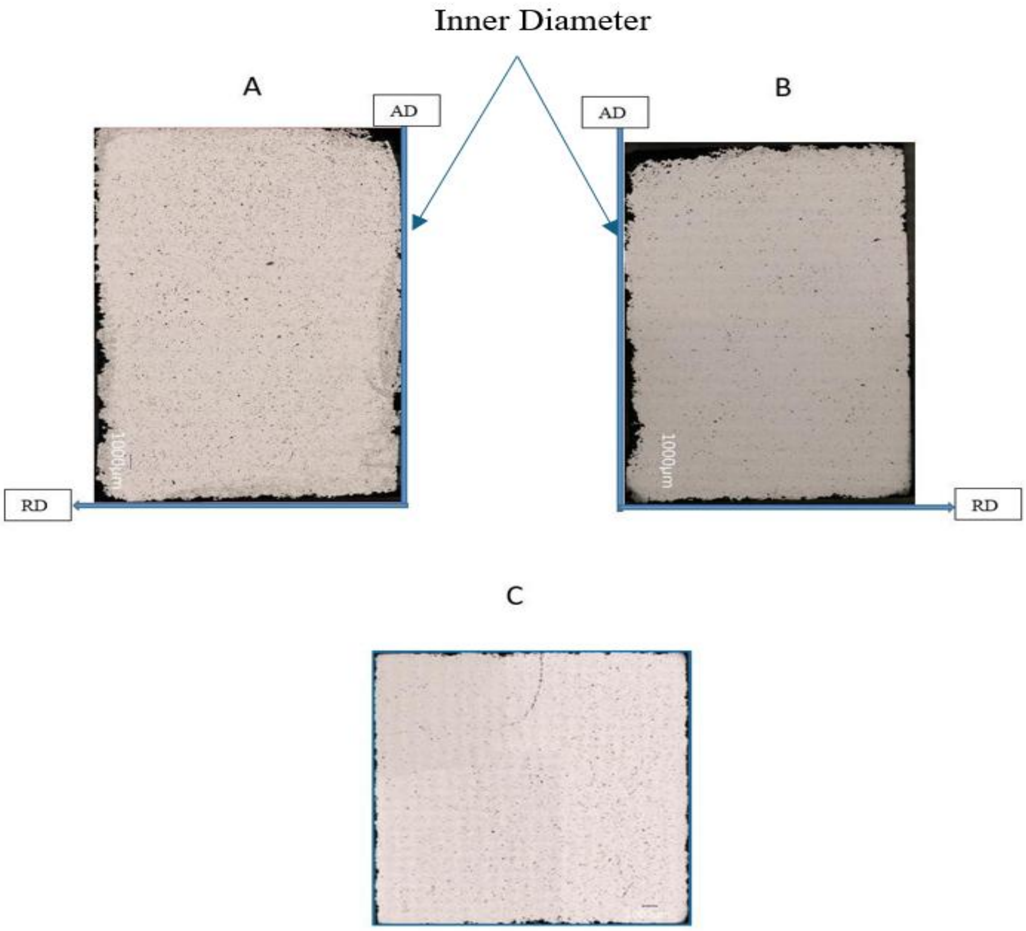

Figure 10.Optical micrographs of Sample 1 (A), Sample 2 (B), and Sample 3 (C). The images illustrate both radial and axial directions

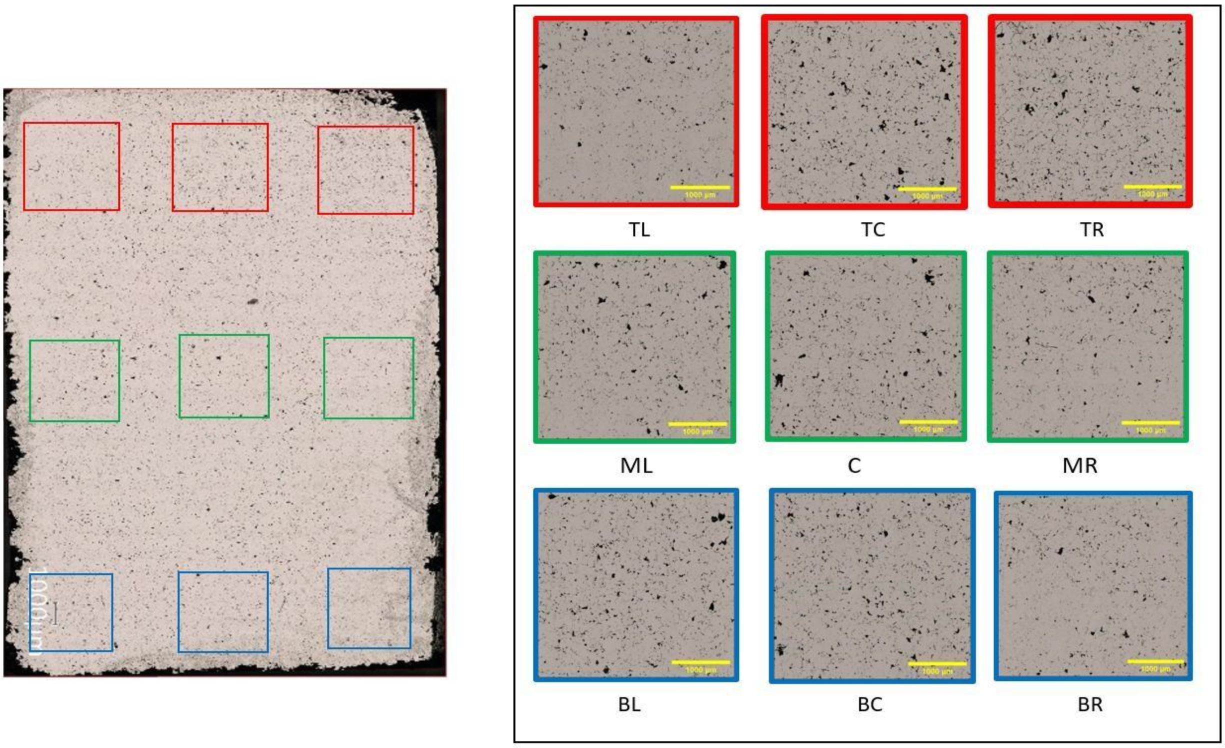

Figure 11.Optical micrographs of Sample 1 (Stator Tooth) captured at nine distinct regions, illustrating surface morphology. TL-Top left, TC-Top center, TR-Top right, ML-Middle left

4.2 Particle Size Distribution

In the stator ring samples, distinct radial and axial trends are observed. Particle distributions for the three samples are obtained using image thresholding (Figure 12). For Sample 1 (Figure 13 A), the top and bottom regions shows consistent trend where the average particle area is highest near the inner diameter (right end) approximately 14000 µm² and 9000 µm² this value then decreases toward the center about 12000 µm² and 6400 µm² followed by slight increase at the outer diameter (left end) reaching around, at 13800 µm² and 6500 µm² respectively. However, in the middle region the inner (9100 µm²) and outer (9200 µm²) diameter shows the highest average particle area when compared to the center (1100 µm²). This gradient suggests a compaction pressure imbalance and potential particle movement towards the die center during pressing. The rightward increase in particle area, seen in both the top and bottom layers, further supports this interpretation

In sample 2 (Figure 13 B), the top, middle, and bottom region shows a consistent trend, where the average particle area are highest near the inner diameter approximately 12,000 µm², 9,500 µm², and 6,500 µm², respectively. This value then decreased towards the center of each layer to about 8,500 µm², 8,000 µm², and 6,300 µm², followed by a slight increase in the outer diameter, reaching around 9,500 µm², 8,000 µm², and 5,600 µm², respectively. Although more uniform than Sample 1, the distribution still reflects non-uniform powder packing, caused by ring geometry and compaction constraints. Notably, the inner diameter of both stator samples demonstrated higher variability, possibly due to frictional resistance or flow hindrance during powder filling.

In contrast, Sample 3 (Figure 13 C), a cube specimen are fabricated using a moving die, demonstrated a significantly more uniform area distribution. Particle areas across top and bottom region shows same trend where the average particle area is highest at left end approximately 2500 µm² and 2900 µm² and decrease towards the center about 1900 µm² and 2300 µm² followed by slightly increase at the right end 2200 µm² and 2500 µm² whereas the middle region has slightly elevated value of 5200 µm² particularly on the right side. Despite this minor variation, the particle area across Sample 3 remained within a tight and consistent range, reflecting uniform compaction pressure and homogeneous powder distribution. The minimal deviation observed confirms the advantage of symmetric geometry and dynamic die motion in producing structurally consistent SMC components.

In summary, the area-based particle size analysis highlights critical differences driven by sample geometry and compaction method. Stator ring samples (1 and 2) exhibited radial gradients and top region demonstrated heavy distributions, especially near the inner diameter, pointing to asymmetric pressure transmission and material movement during pressing. In contrast, the cube sample (Sample 3) displayed excellent uniformity, underscoring the benefits of a controlled, symmetric compaction system.

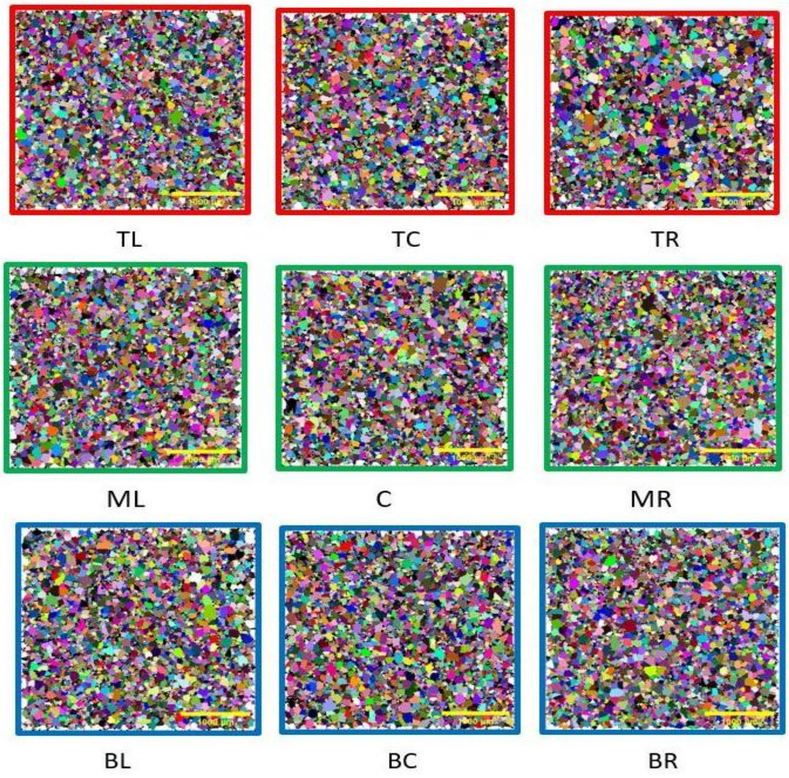

Figure 12.Particle detection results for Sample 1 at nine locations using image thresholding. Thresholding enabled the isolation of individual particles from the background

A

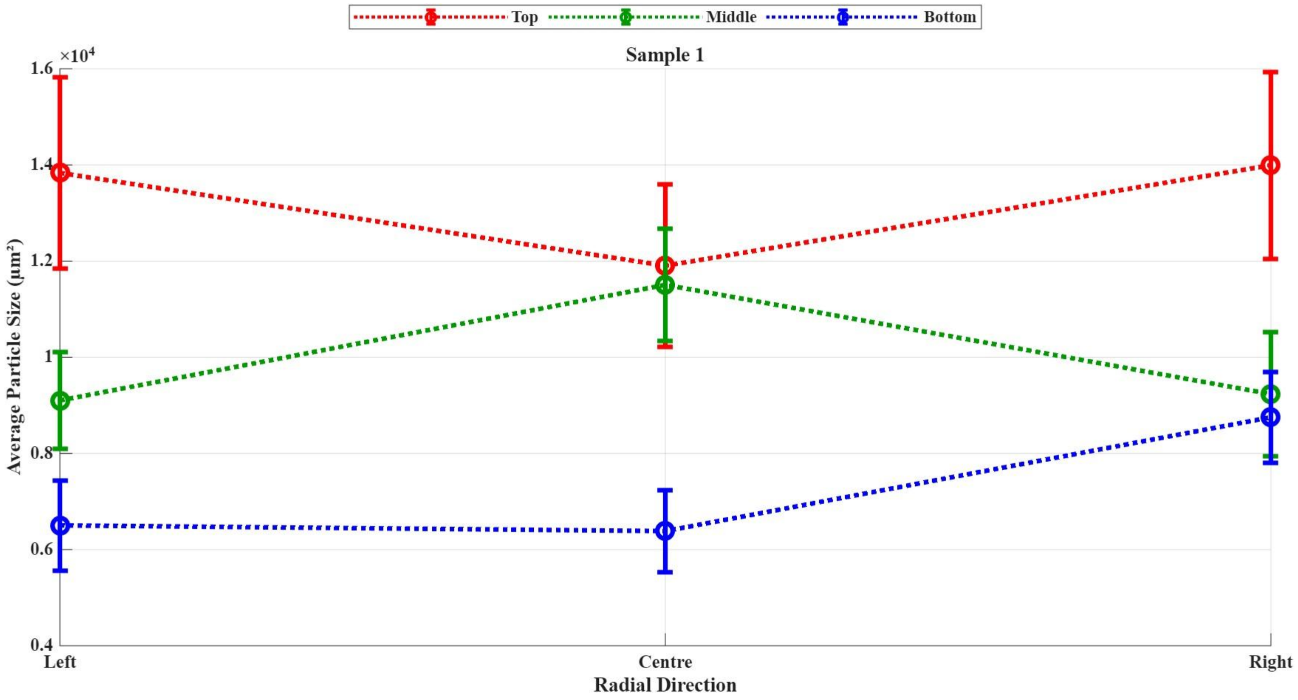
Top
Middle
Bottom
Sample 1
×10^4
1.6
1.4
1.2
1
0.8
0.6
0.4
Average Particle Size (μm²)
Left
Centre
Right
Radial Direction

B

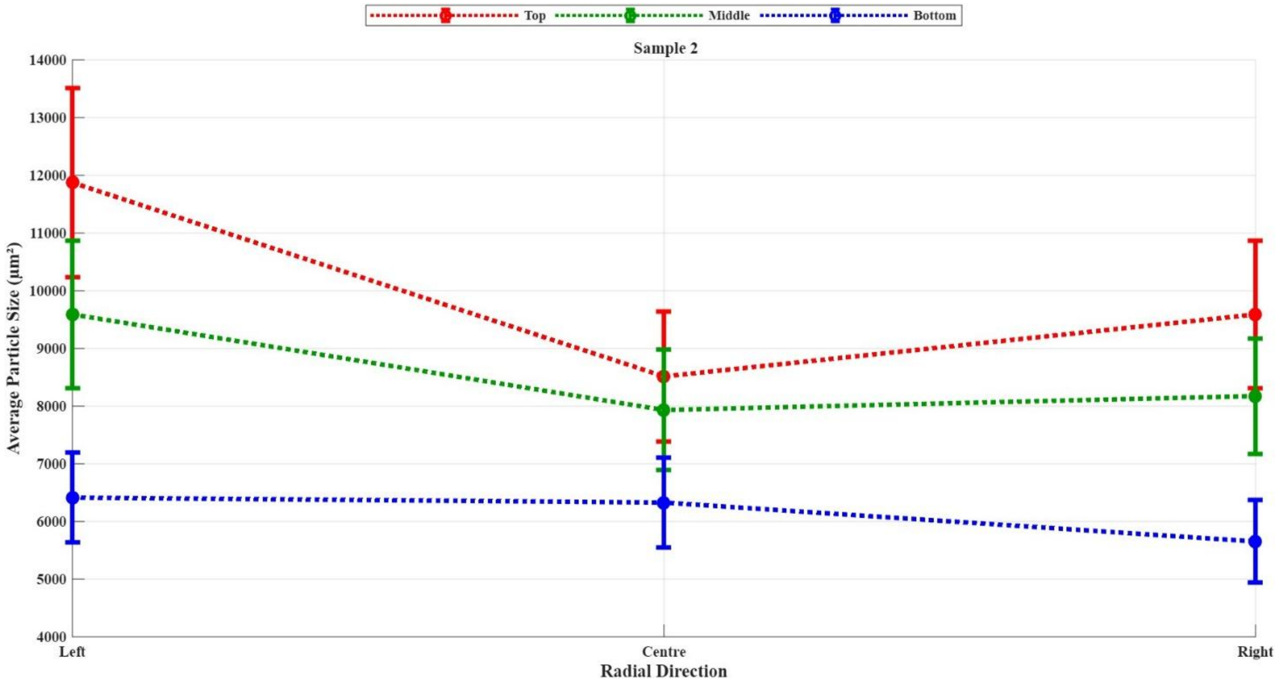
Top
Middle
Bottom
Sample 2
14000
13000
12000
11000
10000
9000
8000
7000
6000
5000
4000
Average Particle Size (μm²)
Left
Centre
Right
Radial Direction

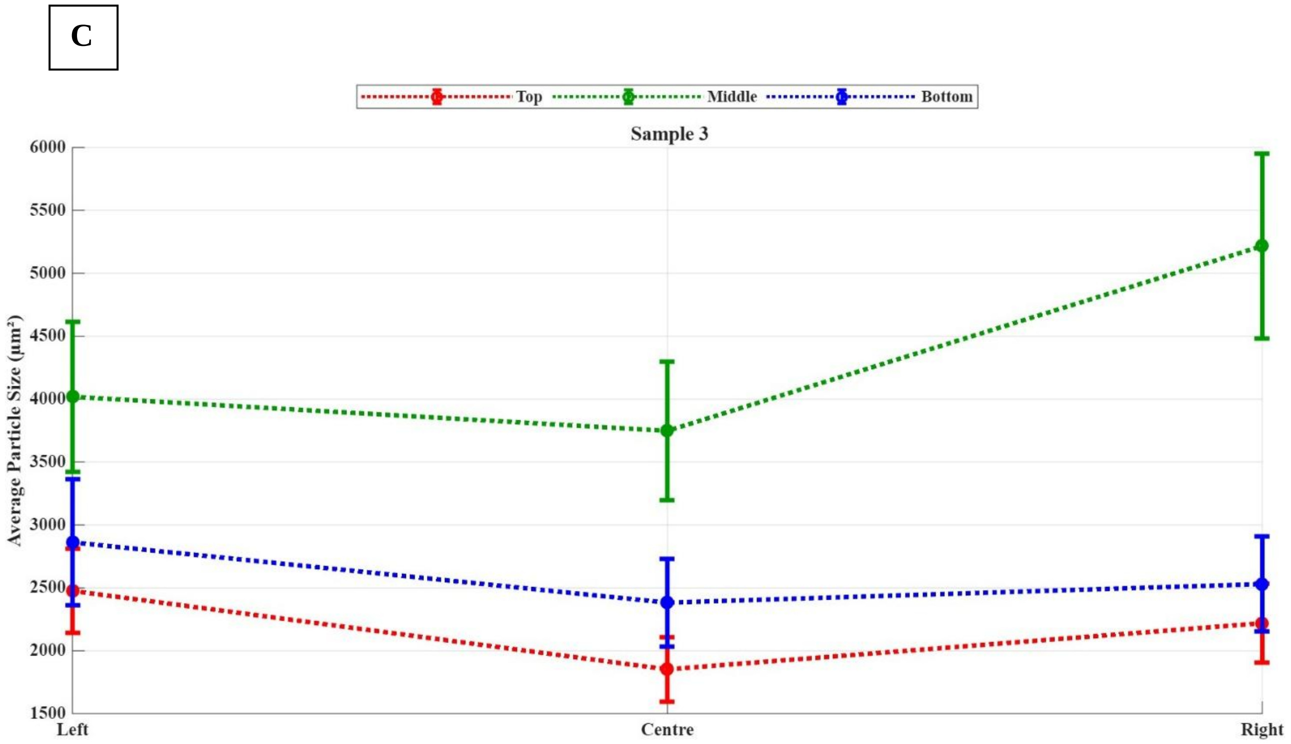

Figure 13.Average particle area distribution for Samples 1(A), 2(B), and 3(B). The graph illustrates variations in particle size across the regions within each sample, highlighting the effect of compaction.

4.3. Coating Area Distribution

The microscope images also provided insight into the binder phase used to coat individual iron particles. The binder appeared as a thin non-metallic phase at the grain boundaries (Figure 14), which electrically insulates adjacent particles. The image thresholding reveales regions of binder presence, typically visible as lighter areas at the inter-particle boundaries.

In Sample 1 (Figure 15A), the highest coating percentage are seen at the center for the top, middle and bottom regions at 11%, 14.4% and 16% respectively, whereas the inner (9.6%, 13.3%, 15.5% respectively) and outer diameter (9.6%, 14.1%, 15.4% respectively) across the top, middle and bottom regions, showed more consistent percentage. This suggests non-uniform settling of the coating material during powder compaction

In Sample 2 (Figure 15B) a similar trend are observed, where the highest coating percentages are seen at the center for all the three regions at 10.7%, 11.6% and 13.6% respectively. However both the inner (9.3%. 11.1%, 13.7% respectively) and outer diameter (10.1%, 10.9%, 13.3% respectively) had relatively lower values for all the three regions. This radial and vertical distribution pattern suggests that powder movement toward the inner diameter or reduced pressure transfer at the outer diameter may contribute to slight coating drift.

Sample 3 (Figure 15C) displayed uniform coating distribution. The highest coating distribution are again seen at the center for the three regions at 15.7%, 13.1% and 15% respectively. However the right (15.6%,12.3% and 14.7% respectively) and left end (15.4%, 12.9% and 13.5% respectively) shows a consistent trend for the three regions The uniform radial profile reveals minimal material drift indicating that this sample benefited from optimized processing, likely including better powder flow and compaction balance.

Overall, the coating percentage data illustrates a clear trend in distribution quality across the three samples. The highest values are observed at the center for all three regions. Sample 1 exhibited pronounced vertical and radial inconsistencies, likely resulting from uneven compaction forces during pressing. In contrast, Sample 2 demonstrated improved coating uniformity. However, some asymmetry particularly along the axial direction. Sample 3 shows the most uniform and consistent coating distribution with minimal fluctuation across both vertical and radial directions, making it the more optimized sample in terms of insulation.

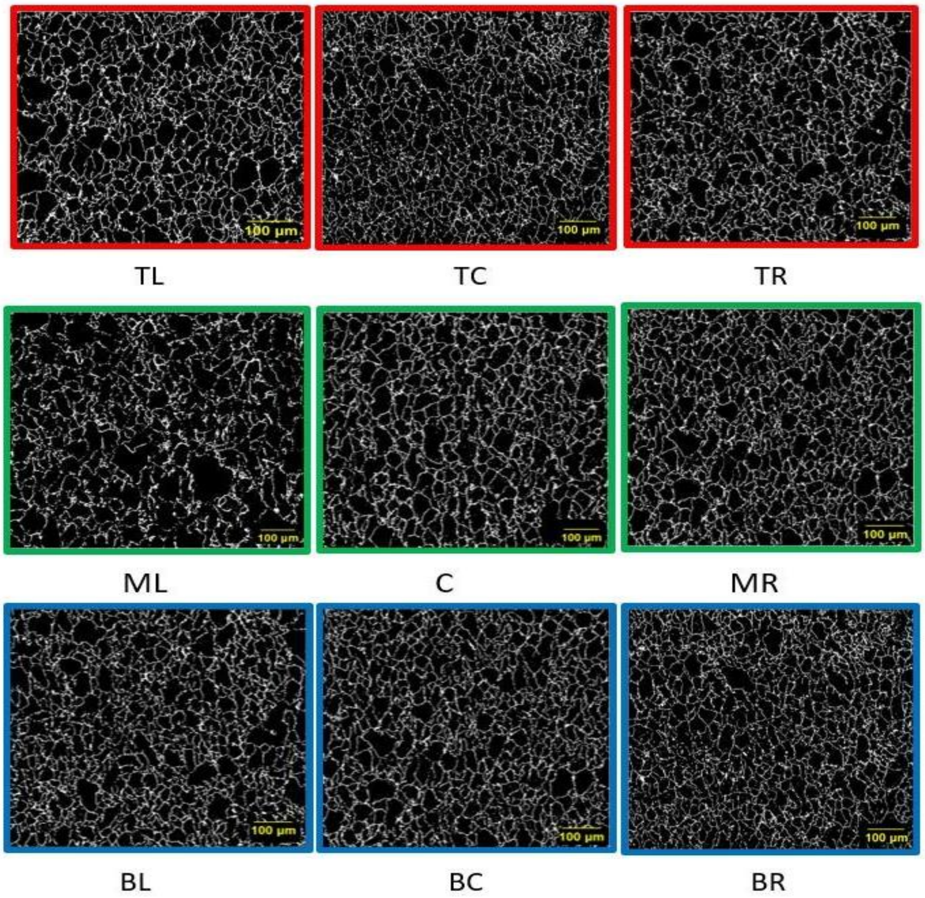

Figure 14.Binder detection results for Sample 1 at nine locations using image thresholding. Thresholding enabled the visualization and isolation of the binder phase coating individual particles across the regions

A

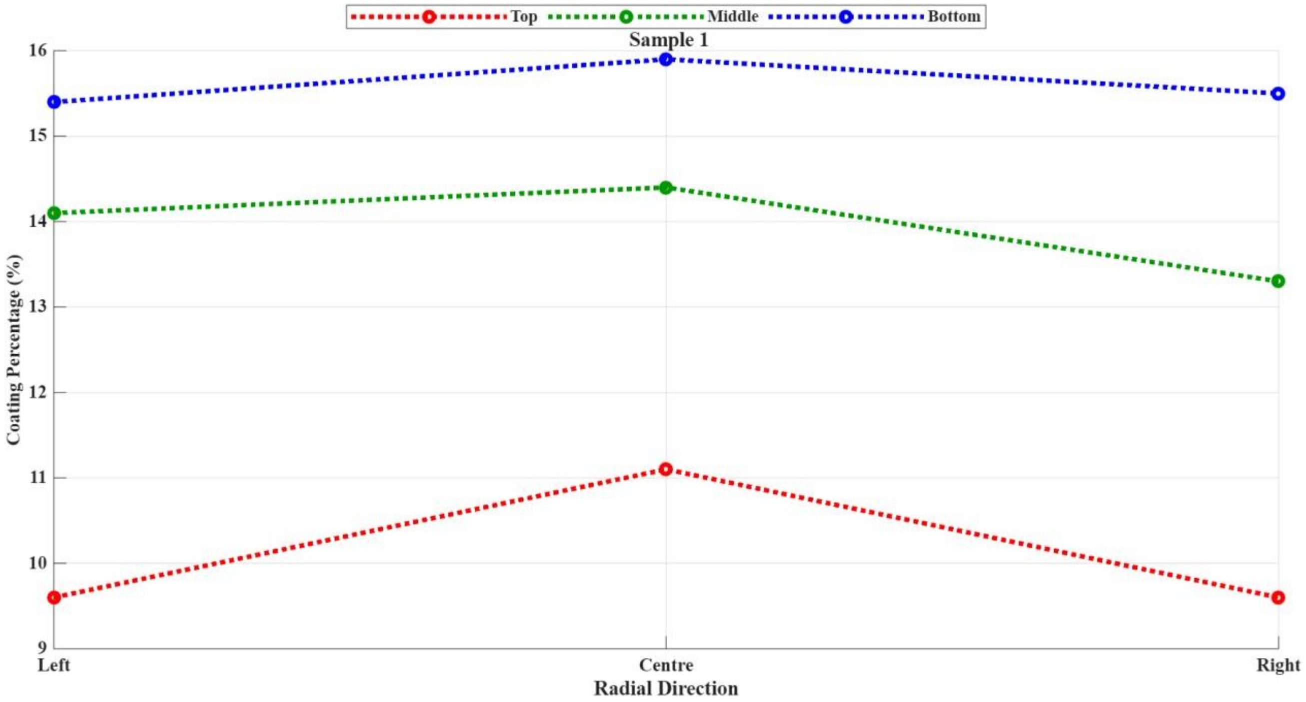
Top
Middle
Bottom
Sample 1
Coating Percentage (%)
16
15
14
13
12
11
10
9
Left
Centre
Right
Radial Direction

B

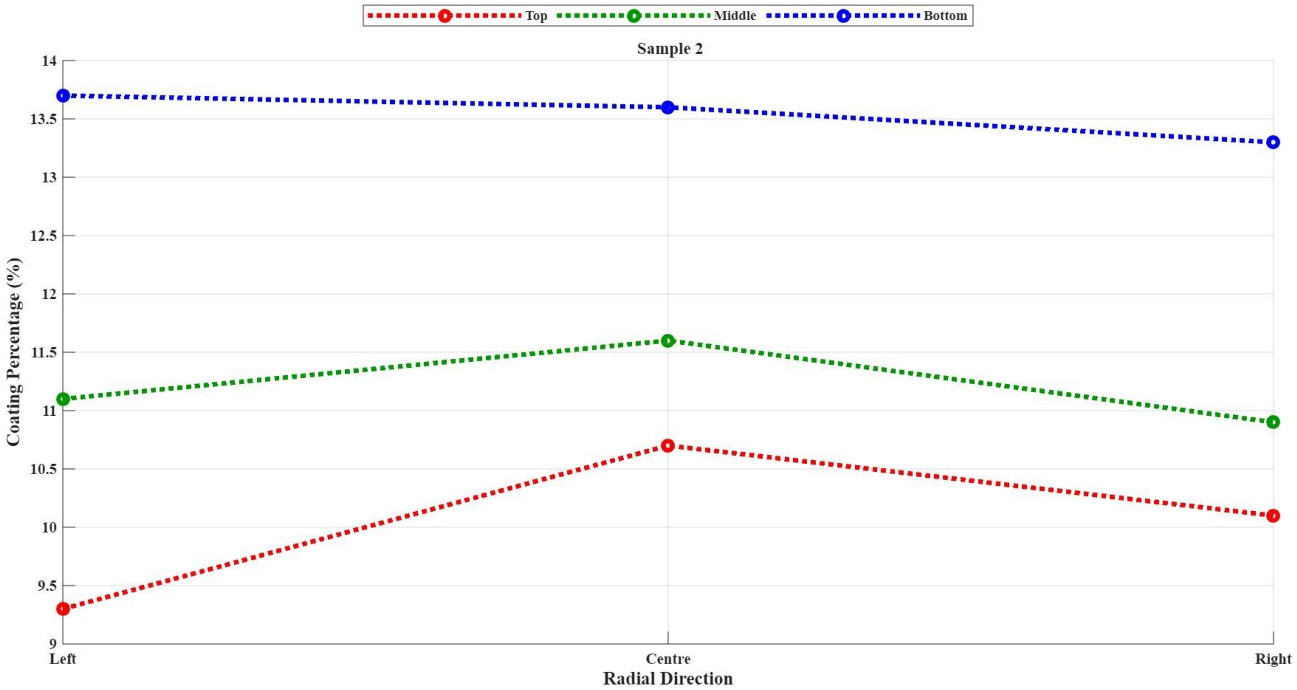
Top
Middle
Bottom
Sample 2
Coating Percentage (%)
14
13.5
13
12.5
12
11.5
11
10.5
10
9.5
9
Left
Centre
Right
Radial Direction

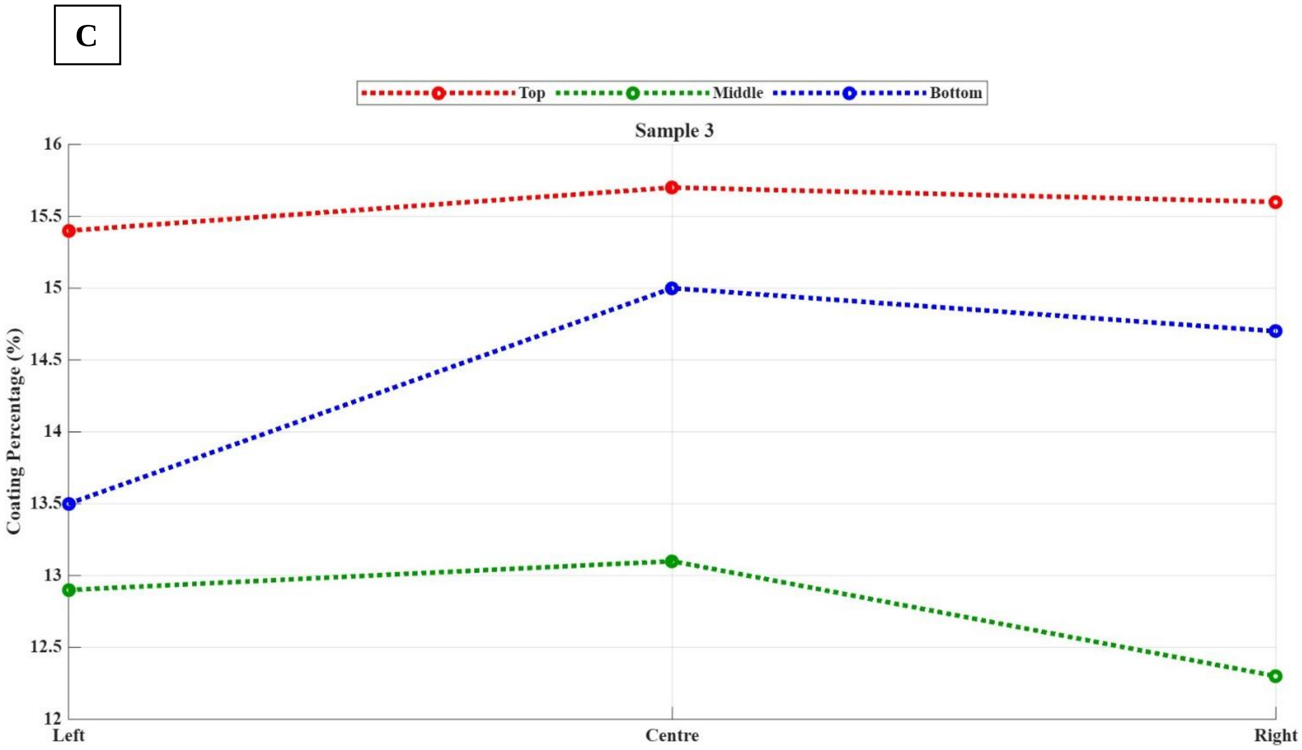

Figure 15.Coating detection results for Samples 1 (A), 2 (B), and 3 (C) at nine locations using image thresholding, illustrating distribution patterns across the regions, and highlighting the effects of compaction.

4.4 Porosity Characterization and Regional Distribution

The optical microscopy image reveals the presence of pores within the SMC sample. Image thresholding technique is used to quantify, isolate, and analyze the pore regions (Figure 16). These pores are irregularly distributed across the surface and It is mostly located along the boundaries of compacted particles. Across all the three samples, the histograms appeared to be right skewed. This indicates that most pores fall within a small size range of 5-20 µm, while a smaller fraction of larger pores are about 50 µm, particularly in some top and center regions. This skewed distribution suggests that fine porosity is present in the structure, indicating non-homogeneous densification during the compaction process.

In Sample 1(Figure 17 A), the highest pore sizes were present at the center of each layer, measuring 17.2 µm in the top, 16.6 µm in the middle, and 16.7 µm in the bottom regions. The outer diameter positions showed values of 16 µm, 16.2 µm, and 16.6 µm, while the inner diameter positions recorded 17.0 µm, 9.4 µm, and 15.6 µm for the top, middle, and bottom layers respectively. The significant drop in the middle-right (outer) region indicates localized densification and non-uniform compaction.

In Sample 2 (Figure 17 B), pore sizes at the center of the top, middle, and bottom layers were 17 µm, 9.5 µm, and 15 µm respectively. The inner diameter recorded 17.2 µm, 15.9 µm, and 16.5 µm, while the outer diameter measured 17.1 µm, 15.6 µm, and 15.7 µm respectively.

In Sample 3 (Figure 17 C), the pore sizes were generally higher and more variable. The center region shows value of 17.1 µm (top), 18.8 µm (middle), and 14.9 µm (bottom). The left edge shows 17.9 µm, 17.5 µm, and 17.2 µm, while the right edge shows 18.7 µm, 15.0 µm, and 10.3 µm respectively. The large pore sizes in the top and middle layers, especially at the center, indicate low compaction resistance, whereas the bottom-right region shows the smallest pore size, pointing to possible die-wall friction and uneven pressure distribution.

In summary, a consistent pattern emerged across the samples, the top layer shows the highest porosity, middle layer shows localized densification (especially in Sample 1 MR and Sample 2 C), and bottom layers are generally more uniform, though Sample 3 introduced notable variability. These observations confirm that compaction pressure is not uniformly transmitted through the sample thickness.

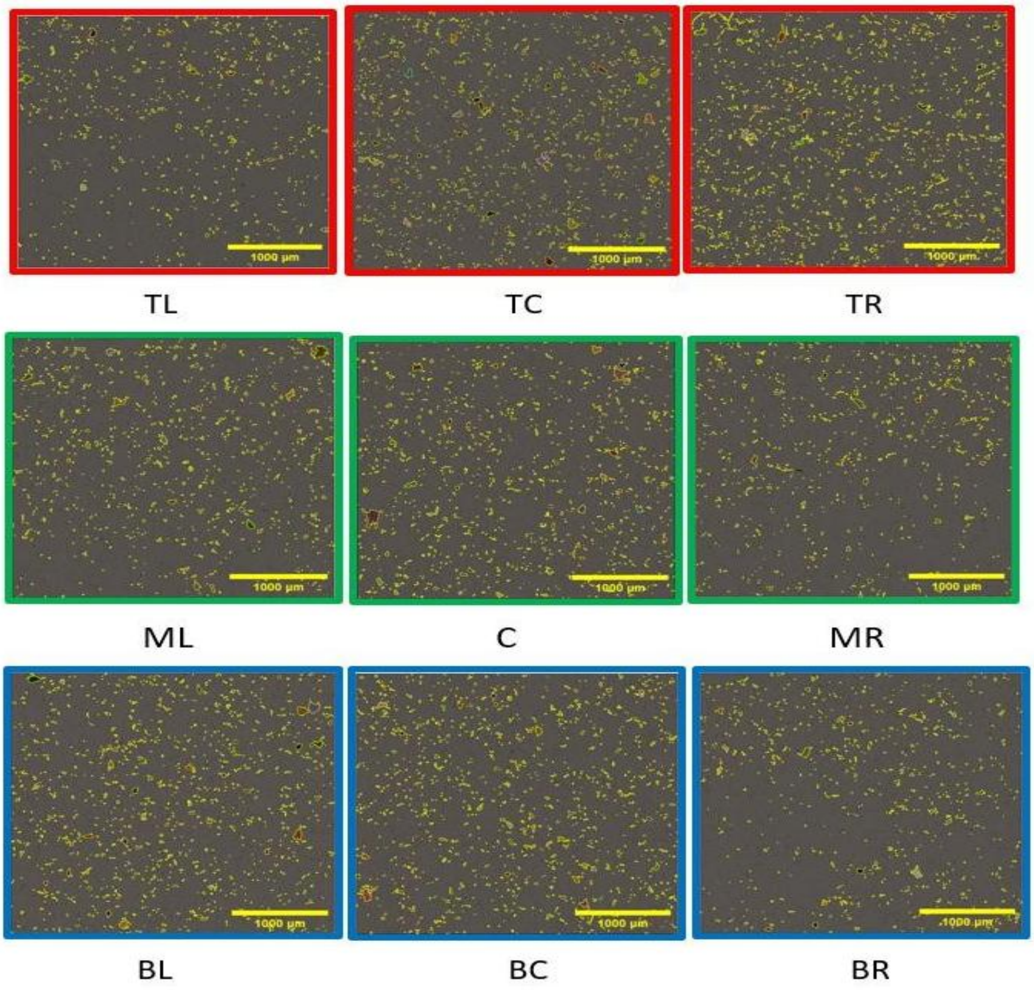

Figure 16.Porosity detection results for Sample 1 at nine locations using image thresholding. Thresholding enabled the visualization and isolation of pore regions within the microstructure across the regions.

A

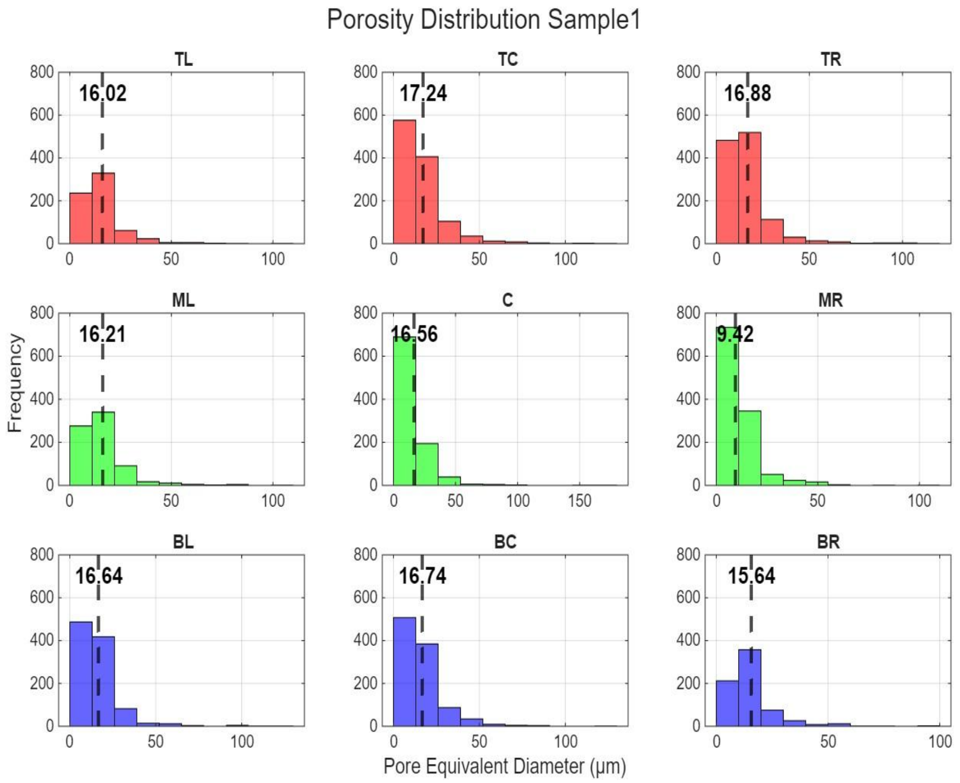
Porosity Distribution Sample1
TL
16.02
TC
17.24
TR
16.88
ML
16.21
C
16.56
MR
9.42
BL
16.64
BC
16.74
BR
15.64
Frequency
0
200
400
600
800
0
50
100
150
Pore Equivalent Diameter (µm)

B

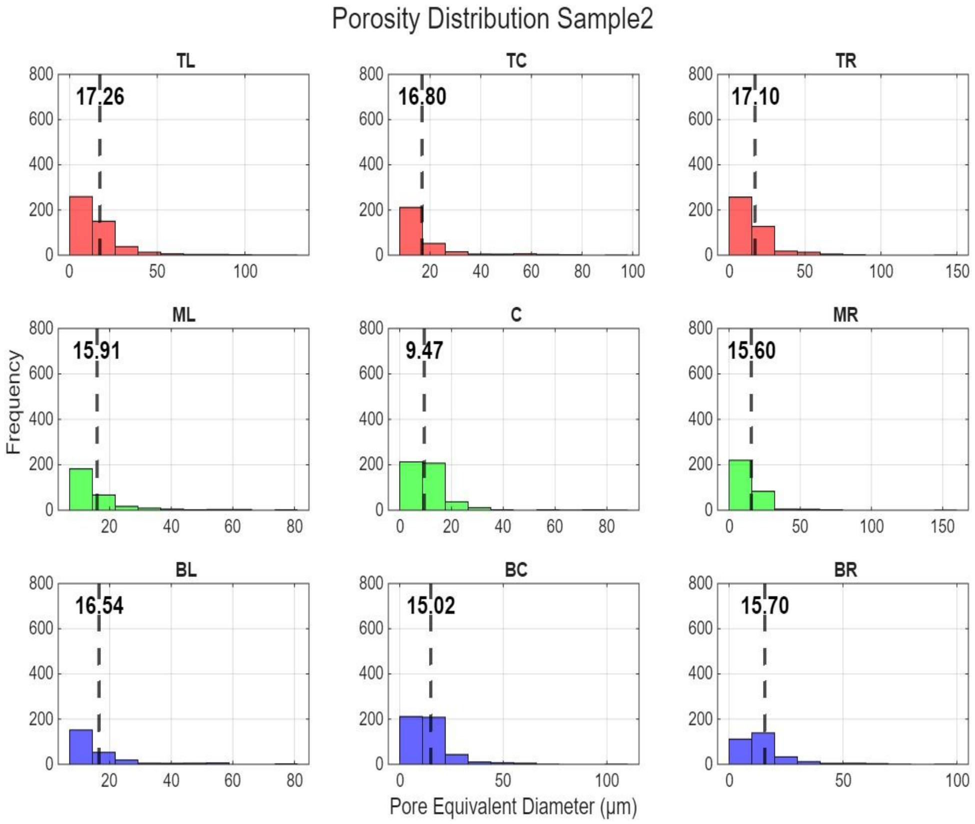
Porosity Distribution Sample2
TL
17.26
TC
16.80
TR
17.10
ML
15.91
C
9.47
MR
15.60
BL
16.54
BC
15.02
BR
15.70
Frequency
0
200
400
600
800
0
20
40
60
80
100
150
Pore Equivalent Diameter (µm)

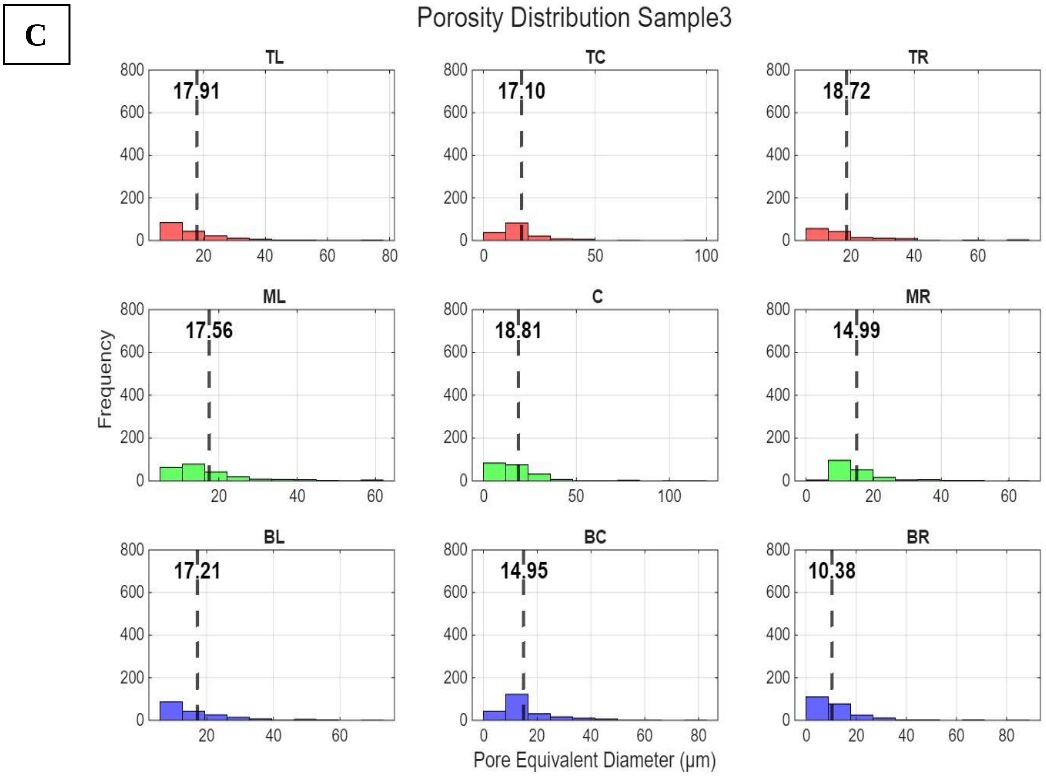

Figure 17.The histograms for Samples 1 (A), 2 (B), and 3 (C) illustrate the distribution of pore equivalent diameters across nine defined regions: top-left (TL), top-center (TC), top-right (TR), middle-left (ML), center (C), middle-right (MR), bottom-left (BL), bottom-center (BC), and bottom - right (BR).

4.4 Influence of Microstructural Characteristics on Electromagnetic Performance of SMCs

The stator tooth magnetic permeability is critically influenced by microstructural factors such as particle size, coating distribution, and porosity. Based on the microstructural data from stator samples 1 and 2, a clear axial gradient is observed across the top, middle, and bottom regions of the stator ring.

In Sample 1, a clear axial gradient in microstructural characteristics appears from the top to the bottom of the stator ring. The top region shows the largest average particle size (1.20×10^4 to 1.40×10^4 μm^2) with high standard deviation, the lowest coating percentage (9.5–11%), and the highest porosity (16.2–17.2 µm pore diameter). This combination supports higher magnetic permeability due to improved particle contact but leads to increased eddy current losses due to insufficient insulation and significant porosity. The middle region displays comparatively balanced values, with particle sizes (0.90×10^4 to 1.15×10^4 μm^2), coating coverage (13.5–14.5%), and porosity (9.4–16.5 µm), which results in more stable magnetic behavior and reduced total iron loss. The bottom region contains the smallest particle sizes (0.65×10^4 to 0.90×10^4 μm^2), the highest coating percentage (15.5–16%), and relatively low porosity (15.6–16.7 µm). This structure reduces eddy current loss but may decrease permeability and increase hysteresis loss due to limited magnetic contact between particles

Sample 2 exhibits a similar axial trend, with slightly smaller particle size ranges overall. The top region contains particle sizes between 0.9 × 10^4 and 1.2 × 10^4 µm^2, low coating percentages (9.5–10.7%), and high porosity values (16.8–17.2 µm), which contribute to higher permeability but also increase eddy current loss due to poor insulation and porosity. The middle region maintains comparatively more balanced microstructure, with particle sizes ranging from 0.8 × 10^4 to 1.0 × 10^4 µm^2, coating percentages of 11–12%, and pore diameters between 9.4 and 15.9 µm. This region provides stable magnetic performance iron losses. The bottom region shows the smallest particle sizes (0.5 × 10^4 to 0.8 × 10^4 µm^2), the highest binder coverage (13–14%), and porosity between 15.0 and 16.5 µm. While High levels of insulation reduce the formation of eddy currents, the reduced particle connectivity limits magnetic permeability and raises hysteresis loss.

The stator tooth shows a clear axial gradient in microstructural characteristics from the top to the bottom of the stator ring, influencing their electromagnetic performance. In both samples, the top region features the largest particle sizes, lowest coating percentages, and highest porosity, promoting higher magnetic permeability but also increased eddy current loss due to poor insulation. The middle region shows comparatively more balanced microstructural values, offering stable magnetic behavior and reduced total iron loss. The bottom region, with smallest particle sizes, highest coating levels, and lower porosity, effectively minimizes eddy current loss but may reduce permeability and increase hysteresis loss due to restricted magnetic contact.

Conclusion

This study aimed to investigate the microstructural characteristics of Soft Magnetic Composites (SMCs) by analyzing particle size, coating distribution, and pore structure across various regions within differently shaped samples. Using high-resolution micrographs and quantitative image analysis across stator ring sections and a cube sample,The study effectively identified and analyzed key microstructural features that influence the electromagnetic performance of the stator. The results revealed clear dependencies between sample geometry, compaction technique, and local structural properties, confirming the critical role of fabrication methods in determining microstructural uniformity.

Stator ring samples (Samples 1 and 2) exhibited pronounced radial and axial non-uniformities, particularly near the top regions and inner diameters. These variations are indicative of uneven compaction pressure transmission and possible powder settling or frictional resistance during die filling. As a result, the samples showed inconsistent particle dispersion, larger localized pores, and uneven coating coverage factors that can negatively impact both the mechanical strength and magnetic efficiency of the components.

In contrast, the cube specimen (Sample 3), demonstrated significantly improved structural uniformity. Across all analyzed regions, particle size distribution, coating area, and porosity remained consistent. This highlights the effectiveness of symmetric geometry and moving-die compaction in minimizing defects and achieving homogeneous microstructures. These results support the conclusion that fixed die pressing in asymmetrical geometry introduces microstructural heterogeneity. While optimized, geometry-specific compaction strategies are essential for ensuring the functional reliability of SMCs.

In conclusion, the work establishes that optimized compaction strategy and geometry-specific process control are essential for achieving homogeneous SMC structures. Improved coating distribution, narrow particle size variation, and balanced porosity contribute to reduced core losses and enhanced magnetic permeability. The study provides a solid foundation for future efforts to refine die design, introduce dual-action pressing, and implement real-time process monitoring for the manufacturing of high-performance SMC components

Future work

Future research should aim to establish correlations between the observed microstructural features such as pore size, shape, and distribution and the magnetic and mechanical properties of SMCs, including permeability and core losses. Employing advanced three-dimensional imaging techniques SEM would enable more comprehensive analysis of pore volume, connectivity, and anisotropy. Further studies should explore the effects of varying compaction pressure, pressing speed, and die-wall friction on porosity gradients, supported by finite element modeling (FEM) to simulate compaction behavior. Expanding the investigation to include different material grades, particle sizes, and coating compositions would help validate the consistency of the observed trends. Additionally, examining the impact of post-compaction processes like annealing on pore closure and magnetic performance would provide practical insights.

Reference

[1] Olabi, A. G., et al. "Battery electric vehicles: Progress, power electronic converters, strength (S), weakness (W), opportunity (O), and threats (T)." International Journal of Thermofluids 16 (2022): 100212.

[2] Electric Machines and Drives Conference, 2003. IEMDC'03.. Vol. 1. IEEE, 2003.

[3] Hultman, L. O., and A. G. Jack. "Soft magnetic composites-materials and applications." IEEE International

[4]Upadhayay, Pranshu. Electrical machine designs based on 3D flux paths with reuse & recycle magnet concepts for automotive applications. Diss. Université Grenoble Alpes, 2018.

[5]Asari, Ashraf Rohanim Binti. Magnetic properties measurement of new magnetic material: SOMALOY 700 (5P). Diss. University of Technology Sydney (Australia), 2018.

[6]Ten, Chee-Wooi, and Yunhe Hou. Modern power system analysis. CRC Press, 2024.

[7]Ye, Zhou, and Björn Skårman. "The effect of manufacturing processes on the properties of multi-layer coated SMC components." PM2016, Hamburg, Germany (2016).

[8]Upadhyaya, Gopal S. Powder metallurgy technology. Cambridge Int Science Publishing, 1997.

[9]Gelinas, C., et al. "Properties and processing of improved SMC materials." Advances in Powder Metallurgy and Particulate Materials 2 (2005): 9.

[10]Fischmeister, Hellmut F. "Powder compaction: fundamentals and recent developments." Proceedings of the Institution of Mechanical Engineers 196.1 (1982): 105-121.

[11] Oikonomou, Christos. On surface characteristics and microstructural development of soft magnetic composite powder and components. Chalmers Tekniska Hogskola (Sweden), 2015.

[12] Lebhard, Anna. Evaluation of an SMC powder during uniaxial compaction and subsequent annealing treatment. Diss. Wien, 2021.

[13]Choi, Moosung, et al. "The effects of Fe nano-powders on compaction behaviors and magnetic properties of SMCs." Journal of Magnetism and Magnetic Materials 480 (2019): 33-39.

[14]Ferraris, Luca, Emir Pošković, and Fausto Franchini. "New soft magnetic composites for electromagnetic applications with improved mechanical properties." AIP Advances 6.5 (2016).

[15] Hughes, Austin, and Bill Drury. Electric motors and drives: fundamentals, types and applications. Newnes, 2019.

[16] Boldea, Ion. "Electric generators and motors: An overview." CES Transactions on Electrical Machines and Systems 1.1 (2017): 3-14.

[17] Kim, Sang-Hoon. Electric motor control: DC, AC, and BLDC motors. Elsevier, 2017.

[18] Husain, Iqbal, et al. "Electric drive technology trends, challenges, and opportunities for future electric vehicles." Proceedings of the IEEE 109.6 (2021): 1039-1059.

[19] Etukudoh, Emmanuel Augustine, et al. "Mechanical engineering in automotive innovation: A review of electric vehicles and future trends." International Journal of Science and Research Archive 11.1 (2024): 579-589.

[20]Deepak, Kritika, et al. "In-wheel motor drive systems for electric vehicles: State of the art, challenges, and future trends." Energies 16.7 (2023): 3121.

[21]Huang, Rundong, et al. "Overview of axial-flux machines and modeling methods." IEEE Transactions on Transportation Electrification 8.2 (2022): 2118-2132.

[22]Chalmers, Brian John, ed. Electric motor handbook. Elsevier, 2013.

[23]Tong, Wei. Mechanical design and manufacturing of electric motors. CRC press, 2022

[24]Toliyat, Hamid A., and Gerald B. Kliman. Handbook of electric motors. CRC press, 2018.

[25] Poskovic, Emir. "Innovative magnetic materials for the new applications in electrical machines." (2019).

[26]Nasiru, Aliyu. Loss Reduction in Axial Flux Machines using Magnetic Shielding. Diss. Newcastle University, 2021.

[27]Huang, Yunkai, et al. "Comparative study of high-speed PM motors with laminated steel and soft magnetic composite cores." 2007 IEEE Industry Applications Annual Meeting.

[28] Jahns, Thomas M., and Hang Dai. "The past, present, and future of power electronics integration technology in motor drives." CPSS Transactions on Power Electronics and Applications 2.3 (2017): 197-216.

[29] Liao, Chendong, Nicola Bianchi, and Zhuoran Zhang. "Recent Developments and Trends in High-Performance PMSM for Aeronautical Applications." Energies 17.23 (2024): 6199.

[30] Shokrollahi, H. E. J. K., and K. Janghorban. "Soft magnetic composite materials (SMCs)." Journal of Materials Processing Technology 189.1-3 (2007): 1-12.

[31] Fernando, Nuwantha, and Fuad Hanin. "Magnetic materials for electrical machine design and future research directions: A review." 2017 IEEE International Electric Machines and Drives Conference (IEMDC). IEEE, 2017.

[32] Rodriguez-Vargas, Bryan Ramiro, et al. "Recent advances in additive manufacturing of soft magnetic materials: A review." Materials 16.16 (2023): 5610.

[33]Bittner, Florian, et al. "The impact of post-processing heat treatment on the magnetic properties of additively manufactured Nd-Fe-B magnets." Journal of Magnetism and Magnetic Materials 603 (2024): 172238.

[34]Solé, Domingo Biel, and Enric Fossas Colet. "SMC applications in power electronics." Variable structure systems: from principles to implementation 66 (2004): 265-293.

[35]Patterson, Dean J., et al. "A comparison of radial and axial flux structures in electrical machines." 2009 IEEE International Electric Machines and Drives Conference. IEEE, 2009.

[30,]Scheerlinck, Bart, Herbert De Gersem, and Peter Sergeant. "3-D eddy current and fringing-flux distribution in an axial-flux permanent-magnet synchronous machine with stator in laminated iron or SMC." IEEE Transactions on Magnetics 51.11 (2015): 1-4.

[31]Reihanian, M., et al. "Application of neural network and genetic algorithm to powder metallurgy of pure iron." Materials & Design 32.6 (2011): 3183-3188

[32] [9]Chin, G. "Review of magnetic properties of Fe-Ni alloys." IEEE Transactions on Magnetics 7.1 (2003): 102-113.

[33]Ding, J., et al. "Microstructure and soft magnetic properties of nanocrystalline Fe–Si powders." Journal of alloys and compounds 314.1-2 (2001): 262-267.

[34]Sourmail, T. "Near equiatomic FeCo alloys: Constitution, mechanical and magnetic properties." Progress in Materials Science 50.7 (2005): 816-880.

[35]Gelinas, C., et al. "Properties and processing of improved SMC materials." Advances in Powder Metallurgy and Particulate Materials 2 (2005): 9.

[36]Nikas, Dimitrios. "Characterization of electrically insulating coatings for soft magnetic composite materials by means of surface sensitive analytical techniques." (2014).

[37] Stipsitz, J., et al. "Structuring metallic coatings to reduce eddy currents and thermal noise in super insulation." Journal of Physics: Conference Series. Vol. 507. No. 4. IOP Publishing, 2014.

[38] Lu, Shuhan, Minggang Wang, and Zhankui Zhao. "Recent advances and future developments in Fe-based amorphous soft magnetic composites." Journal of Non-Crystalline Solids 616 (2023): 122440.

[39]Sidky, P. S., and M. G. Hocking. "Review of inorganic coatings and coating processes for reducing wear and corrosion." British Corrosion Journal 34.3 (1999): 171-183.

[40] Nie, Min, et al. "Multicomponent soft magnetic alloys for soft magnetic composites: A review." Materials Today Electronics (2025): 10015.

[41] Swift, K. G., and J. D. Booker. Manufacturing process selection handbook. Butterworth-Heinemann, 2013.

[42]Todd, Robert H., Dell K. Allen, and Leo Alting. Fundamental principles of manufacturing processes. Industrial Press Inc., 1994.

[43] Creese, Robert. Introduction to manufacturing processes and materials. CRC Press, 2017.

[44] Klocke, Fritz, and Aaron Kuchle. Manufacturing processes. Vol. 2. Berlin: Springer, 2009.

[45] Bai, Yu, et al. "A review on high velocity compaction mechanism of powder metallurgy." Science Progress 104.2 (2021): 00368504211016945.

[46] Fischmeister, Hellmut F. "Powder compaction: fundamentals and recent developments." Proceedings of the Institution of Mechanical Engineers 196.1 (1982): 105-121.

[47] [13]Ahmed, Nabeel, and Glynn J. Atkinson. "A review of soft magnetic composite materials and applications." 2022 International Conference on Electrical Machines (ICEM). IEEE, 2022.

[48] Oberacker, Rainer. "Powder compaction by dry pressing." Ceramics Science and Technology 3 (2012): 3-37.

[49] Briscoe, B. J., and S. L. Rough. "The effects of wall friction in powder compaction." Colloids and Surfaces A: Physicochemical and Engineering Aspects 137.1-3 (1998): 103-116.

[50] Wikman, Bengt, et al. "Wall friction coefficient estimation through modelling of powder die pressing experiment." Powder metallurgy 43.2 (2000): 132-138.

[51] Khoei, A. R., et al. "Mechanical characteristics of die-wall friction on the compaction process of metal nano-powders." Powder Technology 444 (2024): 119987.

[52] Rosato, A. D., T. Vreeland, and F. B. Prinz. "Manufacture of powder compacts." International materials reviews 36.1 (1991): 45-79.

[53] Rahman, Md Mujibur, S. S. M. Nor, and H. Y. Rahman. "Investigation on the effect of lubrication and forming parameters to the green compact generated from iron powder through warm forming route." Materials & Design 32.1 (2011): 447-452.

[54] Higashitani, Ko, Hisao Makino, and Shuji Matsusaka, eds. Powder technology handbook. CRC Press, 2019.

[55] Kuhn, Howard, ed. Powder metallurgy processing: the techniques and analyses. Elsevier, 2012.

[56] Bai, Yu, et al. "A review on high velocity compaction mechanism of powder metallurgy." Science Progress 104.2 (2021): 00368504211016945.

[57] Dixit, Manish, and R. K. Srivastava. "Effect of compaction pressure on microstructure, density and hardness of Copper prepared by Powder Metallurgy route." IOP conference series: materials science and engineering. Vol. 377. No. 1. IOP Publishing, 2018.

[58] Kulkarni, Harshal, Vikram V. Dabhade, and Carl Blais. "Analysis of machining green compacts of a sinter-hardenable powder metallurgy steel: A perspective of material removal mechanism." CIRP Journal of Manufacturing Science and Technology 41 (2023): 430-445.

[59] Ulusoy, Ugur. "A review of particle shape effects on material properties for various engineering applications: from macro to nanoscale." Minerals 13.1 (2023): 91.

[60] Shah, Umang V., et al. "Influence of particle properties on powder bulk behaviour and processability." International journal of pharmaceutics 518.1-2 (2017): 138-154.

[61] Zaamout, Mahmoud. A study of solid lubricants used to prevent wear and friction in powder metallurgy production. Diss. Loughborough University, 1983.

[62] Al-Samarai, Riyadh A., and Yarub Al-Douri. "The Wear." Friction and Wear in Metals. Singapore: Springer Nature Singapore, 2024. 1-31.

[63] Ren, Pengfei, Tung-Chai Ling, and Kim Hung Mo. "Recent advances in artificial aggregate production." Journal of Cleaner Production 291 (2021): 125215.

[64] Ewsuk, K. G. "Powder granulation and compaction." Encyclopedia of Materials: Science and Technology (2001): 7788-78

[65] Pošković, Emir, et al. "Rapid characterization method for SMC materials for a preliminary selection." Applied Sciences 11.24 (2021): 12133.

[66] Dias, M. M., et al. "Influence of resin type and content on electrical and magnetic properties of soft magnetic composites (SMCs)." Powder technology 237 (2013): 213-220.

[67] Goodenough, John B. "Summary of losses in magnetic materials." IEEE Transactions on magnetics 38.5 (2002): 3398-3408.

[68] Rodriguez-Sotelo, Daniela, et al. "Power losses models for magnetic cores: A review." Micromachines 13.3 (2022): 418.

[69] Ueno, Tomoyuki, et al. "Practical and potential applications of soft magnetic powder cores with superior magnetic properties." SEI Technical Review 82.9 (2016).

[70] Liu, Yapi, et al. "Microstructure and magnetic properties of soft magnetic powder cores of amorphous and nanocrystalline alloys." Journal of Magnetism and Magnetic Materials 330 (2013): 119-133.

[71] Verma, Anjali, et al. "Development of a new soft ferrite core for power applications." Journal of Magnetism and Magnetic Materials 300.2 (2006): 500-505.

[72] Skutt, Glenn Richard. High-frequency dimensional effects in ferrite-core magnetic devices. Diss. Virginia Polytechnic Institute and State University, 1996.

[73] Fiorillo, Fausto, et al. "Soft magnetic materials." Wiley Encyclopedia of Electrical and Electronics Engineering. John Wiley & Sons, Inc., 2016. 1-42.

[74] Tseng, King-Jet, and Siang-Beng Wee. "Analysis of flux distribution and core losses in interior permanent magnet motor." IEEE Transactions on Energy Conversion 14.4 (2002): 969-975.[75]Slemon, Gordon R., and Xian Liu. "Core losses in permanent magnet motors." IEEE Transactions on Magnetics 26.5 (1990): 1653-1655.

[76] Haddad, Reemon Z. "Iron loss analysis in axial flux permanent magnet synchronous motors with soft magnetic composite core material." IEEE Transactions on Energy Conversion 37.1 (2021): 295-303.

[77] Potgieter, Johannes HJ, et al. "Effects observed in the characterization of soft magnetic composite for high frequency, high flux density applications." IEEE Transactions on Industrial Electronics 64.3 (2016): 2486-2493.

[78] Alvarez, Kenny L., et al. "Novel Fe-based amorphous and nanocrystalline powder cores for high-frequency power conversion." Journal of Magnetism and Magnetic Materials 501 (2020): 166457.

[79] Bocchini, G. Filippo. "Warm compaction of metal powders: why it works, why it requires a sophisticated engineering approach." Powder metallurgy 42.2 (1999): 171-180.

[80] Dogan, C. P., et al. "Mechanical processing, compaction, and thermal processing of α-Fe powder." Nanostructured materials 4.6 (1994): 631-644.

[81] Wang, Gang, et al. "Eddy current sensor with multiple spatial degrees of freedom for concentrating magnetic fields." IEEE Transactions on Instrumentation and Measurement 72 (2023): 1-11.

[82] Wang, Jian, et al. "Intergranular insulated Fe/SiO2 soft magnetic composite for decreased core loss." Advanced Powder Technology 27.4 (2016): 1189-1194.

[83] McLachlan, David S., Terence B. Doyle, and Godfrey Sauti. "Percolation behaviour in the magnetic permeability and electrical conductivity in conducting magnetic–insulating non magnetic binary composites." Journal of magnetism and magnetic materials 458 (2018): 365-370.

[84] Pittini-Yamada, Y., et al. "Permeability of hybrid soft magnetic composites." Acta Materialia 59.11 (2011): 4291-4302.

[85] Hubert, Alex, and Rudolf Schäfer. Magnetic domains: the analysis of magnetic microstructures. Springer Science & Business Media, 1998.

[86] Hawkes, Peter W., and John CH Spence, eds. Springer handbook of microscopy. Springer Nature, 2019.

[87] Baïlon, Jean-Pierre, and Jean-Marie Dorlot. *Des matériaux*. 3rd ed., Presses internationales polytechniques, 2000

[88] Jähne, Bernd. Digital image processing. Springer Science & Business Media, 2005.

[89] Jain, Anil K. Fundamentals of digital image processing. Prentice-Hall, Inc., 1989.

[90] Chanda, Bhabatosh, and Dwijesh Dutta Majumder. Digital image processing and analysis. PHI Learning Pvt. Ltd., 2011.

[91] Simizu, Satoru, et al. "Flux switching permanent magnet motor with metal amorphous nanocomposite soft magnetic material and rare earth free permanent magnets." *2021 IEEE Energy Conversion Congress and Exposition (ECCE)*. IEEE, 2021.

Appendices

Table 3. Microstructural characterization of Sample1 at different locations (Top Left, Top Center, Top Right), showing image area, particle area, pore area, and coating area in various units (pixels, square microns, fractions, equivalent diameter)

Sample1	Image area	Particle area		Pore area		Coating area	
Location	Top Left	Mean	SD	MEAN	SD	MEAN	SD
Pixels	16000000	32172.0		1207.4		891.2	
Square microns	6970972.8	13834.0	1987.5	269.9	515.3	445.6	1094.98
Fractions	0.43	77.4		2.2		9.6	
Equivalent Diameter		132.71	7.011	16.0	19.1		
Location	Top center						
Pixels	16000000	27684.4		821.4		325	
Square microns	6970972.8	11904.3	1694.5	410.7	939.7	162.5	304.8723
Fractions	0.43	76.7		2.3		11.1	
Equivalent Diameter		123.1	10.5	17.2	24.5		
Location	Top Right						
Pixels	16000000	32539.7					
Square microns	6970972.8	13992.1	1941.8	305.2	557.6	328.1	294.39
Fractions	0.43	75.8		2.7		9.6	
Equivalent Diameter		133.4	6.8	16.8	19.3		
Location	Middle left						
Pixels	16000000	3913.7					
Square microns	6970972.8	9101.8	1009.1	305.8	663.7	125.7	381.01
Fractions	0.43	71.9		1.7		14.1	
Equivalent Diameter		107.65	9.7	16.2	19.7		
Location	center						

Pixels	16000000	26756.5					
Square microns	6970972.8	11505.3	1161.3	383.4	1256.5	359.7	543.1
Fractions	0.43	73.3		1.7		14.4	
Equivalent Diameter		121.0	7.6	16.5	22.7		
Location	Middle right						
Pixels	16000000	21474.4					
Square microns	6970972.8	9234.0	1289.7	263.8	565.69	185.4	631.4
Fractions	0.43	73.67		1.5		13.3	
Equivalent Diameter		108.4	10.2	9.4	18.52		
Location	Bottom left						
Pixels	16000000	15121.6					
Square microns	6970972.8	6502.3	936.1	328.7	603.4	388.6	459.3
Fractions	0.43	72.0		2.0		15.4	
Equivalent Diameter		90.9	10.95	16.6	19.1		
Location	Bottom center						
Pixels	16000000	14846.5					
Square microns	6970972.8	6384.0	671.4	320.4	589.7	227.7	641.0
Fraction	0.43	77.87		2.2		15.9	
Equivalent Diameter		90.1	7.0	16.7	18.8		
Location	Bottom right						
Pixels	16000000	20350.9					
Square microns	6970972.8	8750.9	944.3	275.5	620.2	275.5	578.3
Fractions	0.43	71.3		2.1		15.5	
Equivalent Diameter		105.5	9.4	15.6	18.3		

Table 4. Microstructural characterization of Sample 2 at different locations (Top Left, Top Center, Top Right), showing image area, particle area, pore area, and coating area in various units (pixels, square microns, fractions, equivalent diameter).

Sample2	Image area	Particle area		Pore area		Coating area	
Location	Top Left	Mean	SD	MEAN	SD	MEAN	SD
Pixels	16000000	27617.4					
Square microns	6970972.8	11875.5	1643.5	493.4	953.5	202.84	1162.8
Fractions	0.43	77.6		1.3		9.3	
Equivalent Diameter		122.9	7.8	17.2	28.9		
Location	Top center						
Pixels	16000000	19800.4					
Square microns	6970972.8	8514.2	1124.3	410.0	803.0	190.9	918.9
Fractions	0.43	79.6		0.9		10.7	
Equivalent Diameter		104.1	8.1	16.8	23.58		
Location	Top Right						
Pixels	16000000	22300.9					
Square microns	6970972.8	9589.4	1276.8	339.1	609.72	135.0	465.1
Fractions	0.43	78.8		0.9		10.1	
Equivalent Diameter		110.4	8.2	17.1	20.25		
Location	Middle left						
Pixels	16000000	22300.2					
Square microns	6970972.8	9589.1	1274.6	316.9	550.4	301.49	3107.4
Fractions	0.43	75.7		0.5		11.1	
Equivalent Diameter		110.4	10.6	15.9	22.1		
Location	center						
Pixels	16000000	18447.4					
Square microns	6970972.8	7932.4	1044.9	310.4	743.5	91.977	169.0
Fractions	0.43	74.5		0.5		11.6	
Equivalent Diameter		100.4	9.1	9.4	19.5		
Location	Middle right						
Pixels	16000000						
Square microns	6970972.8	8257.5	706.76	405.34	1493.8	132.9	291.5
Fractions	0.43	71.8		0.5		10.9	
Equivalent Diameter		249	8.9	15.6	23.2		

Location	Bottom left						
Pixels	16000000	19203.4					
Square microns	6970972.8	8174.6	998.1	394.9	654.1	455.64	3984.5
Fractions	0.43	74.1		0.7			
Equivalent Diameter		102.0	9.0	16.5	18.7	13.7	
Location	Bottom center						
Pixels	16000000	14717.2					
Square microns	6970972.8	6328.4	777.7	290.0	616.82	396.1	3392.0
Fraction	0.43	76.68		0.6		13.6	
Equivalent Diameter		89.7	9.1	15.0	19.7		
Location	Bottom right						
Pixels	16000000	13147.2					
Square microns	6970972.8	5653.3	715.6	429.1	829.91	125.7	991.6
Fractions	0.43	78.13		0.6		13.3	
Equivalent Diameter		84.7	9.9	15.7	27.5		

Table 5. Microstructural characterization of Sample 3 at different locations (Top Left, Top Center, Top Right), showing image area, particle area, pore area, and coating area in various units (pixels, square microns, fractions, equivalent diameter).

Sample3	Image area	Particle area		Pore area		Coating area	
Location	Top Left	Mean	SD	MEAN	SD	MEAN	SD
Pixels	16000000	5756.9					
Square microns	6970972.8	2475.5	335.2	219.3	260.1	47.4	306.77
Fractions	0.43	77.2		0.8		15.4	
Equivalent Diameter		56.14	4.9	17.9	12.3		
Location	Top center						
Pixels	16000000	4306.9		362.71	736.5	35.33	484.69
Square microns	6970972.8	1852.0	256.7	1.0		15.7	
Fractions	0.43			17.1	19.7		
Equivalent Diameter		48.5	4.1				
Location	Top Right						
Pixels	16000000	5161.1					
Square microns	6970972.8	2219.3	315.1	335.76	548.93	50.6	296.8
Fractions	0.43	71.8		0.8		15.6	

Equivalent Diameter		53.1	5.5	18.7	19.16		
Location	Middle left						
Pixels	16000000	9344.4					
Square microns	6970972.8	4018.1	594.8	396.7	800.0	62.1	206.0
Fractions	0.43	77.1		1.8		12.9	
Equivalent Diameter		71.5	9.1	17.5	26.7		
Location	center						
Pixels	16000000	8715.8					
Square microns	6970972.8	3747.8	550.1	507.9	1204.9	33.59	354.93
Fractions	0.43	69.5		1.8		13.1	
Equivalent Diameter		69.0	5.72	18.8	27.2		
Location	Middle right						
Pixels	16000000	12130.6					
Square microns	6970972.8	5216.2	735.0	261.2	373.15	60.7	541.8
Fractions	0.43	68.7		1.7		12.3	
Equivalent Diameter		81.4	5.6	14.9	15.48		
Location	Bottom left						
Pixels	16000000	6653.4					
Square microns	6970972.8	2861.0	500.7	298.7	418.64	57.4	488.2
Fractions	0.43	75.8		1.2		13.5	
Equivalent Diameter		60.3	7.2	17.2	16.7		
Location	Bottom center						
Pixels	16000000	5540.4					
Square microns	6970972.8	2382.4	349.9	375.94	679.82	64.9	474.39
Fraction	0.43	66.0		1.7		15.0	
Equivalent Diameter		55.0	5.03	14.9	22.3		
Location	Bottom right						
Pixels	16000000	5885.8					
Square microns	6970972.8	2530.9	376.4	299.01	479.8	69.2	447.23
Fractions	0.43	63.0		1.0		14.7	
Equivalent Diameter		56.7	4.5	10.3	16.3		